(NASA-TM-4111) TRANSONIC NAVIER-STOKES SOLUTIONS OF THREE-DIMENSIONAL AFTERBODY FLOWS (NASA. Langley Research Center) 62 p

N89-23433

CSCL 01A

Unclas

H1/02 0217448

NASA Technical Memorandum 4111

Transonic Navier-Stokes Solutions of Three-Dimensional Afterbody Flows

William B. Compton III, James L. Thomas,
William K. Abeyounis, and Mary L. Mason
Langley Research Center
Hampton, Virginia

National Aeronautics and
Space Administration
Office of Management
Scientific and Technical
Information Division

1989

Summary

The performance of a three-dimensional Navier-Stokes solution technique in predicting the transonic flow past a nonaxisymmetric nozzle has been investigated. The investigation was conducted at free-stream Mach numbers ranging from 0.60 to 0.94 and an angle of attack of 0°. Wind-tunnel data with the jet exhaust simulated by high pressure air were also obtained to compare with the numerical calculations. In the numerical procedure, the jet exhaust is represented by a solid sting.

The numerical solution procedure employs the three-dimensional, time-dependent, Reynolds-averaged Navier-Stokes equations written in strong conservation form, a thin layer assumption, and the Baldwin-Lomax turbulence model. The equations are solved by using the finite-volume principle in conjunction with an approximately factored upwind-biased numerical algorithm.

The Navier-Stokes solution technique predicts the flow over most of the afterbody quite well when no separation is present. Under these conditions, it does a particularly good job of capturing the negative pressure peak as the flow expands around the boattail shoulder. It also successfully predicts vortices which have been experimentally shown to trail from the nonaxisymmetric nozzle. As expected, the procedure does not predict the flow well at the juncture of the nozzle exit and the solid jet plume simulator. This result reiterates the well-established fact that a solid plume simulator does not adequately represent the jet exhaust. With the Baldwin-Lomax turbulence model, the numerical solution procedure also gives poor results when there are strong shocks and large separated areas on the nozzle.

Introduction

When a typical fighter airplane is flying at transonic speeds, 40 to 50 percent of its drag is associated with its afterbody (refs. 1 and 2). In the afterbody region, flows over the fuselage and empennage merge and further interact with the propulsive exhaust to create a complex flow field which strongly influences the aerodynamic characteristics of the airplane. The flow field is rotational and highly interactive; hence viscous effects are very important, especially at off-design conditions.

Traditionally, engineers have utilized wind tunnels to investigate this complicated flow field and derive configurations with desirable flight characteristics. Theoretical methods which would adequately handle the intricate flow phenomena did not exist. Now, however, numerical solution techniques which will compute complicated aerodynamic flows are becoming available and are being used to complement, but not replace, wind tunnels as investigative tools. In general, computational methods more readily yield information about the complete flow field and isolated components than wind tunnels; thus, they are well suited for use in gaining an understanding of the mechanics of the flow and identifying components with undesirable aerodynamic characteristics.

Inviscid, irrotational computational methods have already proven to be useful tools in the design of wings at cruise conditions. (See refs. 3 and 4.) However, for predicting the complex flow field generated in the afterbody region at transonic speeds, Navier-Stokes techniques are needed to adequately simulate the physics of the flow. Examples of Navier-Stokes calculations which have been made for afterbody flows include those of Swanson and Deiwert. Swanson solved the axisymmetric form of the equations for the flow over axisymmetric afterbodies (ref. 5), and the two-dimensional form of the equations for the flow over nonaxisymmetric afterbodies (ref. 6). He solved the three-dimensional equations for the internal flow only (ref. 6). These computations were made on a CDC® CYBER 203 computer using an alternating-direction-implicit numerical algorithm with central differencing to integrate the equations over time and space.

Deiwert solved the axisymmetric form of the Navier-Stokes equations for both transonic and supersonic flow over axisymmetric afterbodies (refs. 7 and 8). He solved the three-dimensional form of the equations for the supersonic flow past a body of revolution with a centered propulsive jet at angle of attack (ref. 9). These solutions were obtained on a CDC® CYBER 205 computer. Deiwert also used an alternating-direction-implicit numerical algorithm with central differencing to integrate the equations.

Recently, advances such as upwind differencing have been made in numerical algorithms for solving the three-dimensional Navier-Stokes equations. See references 10 through 13, for instance. In reference 13, an upwind-biased numerical algorithm was used to solve these equations for the flow over a prolate spheriod at low subsonic Mach numbers and at angle of attack. Although the emphasis was on the whole spheroid, afterbody results were presented. However, in none of these investigations were the three-dimensional Navier-Stokes equations solved for the external afterbody flow at transonic speeds.

The present paper examines the performance of this upwind-biased numerical algorithm in solving the three-dimensional Navier-Stokes equations for the subsonic and transonic flow over a nonaxisymmetric nozzle. It extends the previous work in three

main ways. First, the three-dimensional Navier-Stokes equations are solved for the flow past an afterbody at transonic speeds. Second, the upwinding algorithm is applied to this specific problem. Finally, the application is for a nonaxisymmetric nozzle typical of those being advocated for advanced fighter airplanes. The free-stream test Mach numbers ranged from 0.60 to 0.94, and the angle of attack was 0°. Wind-tunnel data to compare with the numerical calculations were also obtained.

The Navier-Stokes solution procedure used in making the calculations is described in references 10 through 13. In the procedure, the three-dimensional, time-dependent, Reynolds-averaged Navier-Stokes equations are written in strong conservation form and a thin layer assumption is made to simplify the dissipation terms. For the case of a turbulent boundary layer, these terms are simulated with a Baldwin-Lomax turbulence model. The solution procedure operates on the finite-volume principle and employs an approximately factored upwind-biased numerical algorithm to integrate the equations over time and space. For the present calculations, the jet exhaust is represented by a solid sting.

The experimental portion of the investigation was conducted in the Langley 16-Foot Transonic Wind Tunnel. The data presented are part of a broad experimental data base which was obtained for the nonaxisymmetric variable-geometry nozzle described previously. In the wind-tunnel experiment, high pressure air was used to simulate the jet exhaust.

The performance of the numerical Navier-Stokes procedure in predicting the three-dimensional afterbody flow field is assessed over the range of conditions investigated. An assessment is made of the suitability of the Baldwin-Lomax turbulence model to handle the turbulent diffusion in the flow regimes encountered.

Symbols

$\mathbf{A}$	Jacobian matrix of transformed flux vector, $\widehat{\mathbf{F}}$
A_{ref}	reference area, $A_{\text{ref}} = 1.0$
a, b, f, h	dimensions (see fig. 4(c))
C_f	skin friction coefficient, $\frac{\tau_w}{q_\infty}$
C_L	lift coefficient, $\frac{L}{A_{\text{ref}} q_\infty}$
C_D	drag coefficient, $\frac{D}{A_{\text{ref}} q_\infty}$
C_p	pressure coefficient, $\frac{p - p_\infty}{q_\infty}$
C_p^*	critical pressure coefficient
c	speed of sound
c_p	specific heat at constant pressure
D	drag
e	total energy per unit volume
$\mathbf{F}, \mathbf{G}, \mathbf{H}$	flux vector in physical (Cartesian) coordinate direction x, y, and z, respectively
$\widehat{\mathbf{F}}$	flux vector in ξ transformed coordinate direction
$\widehat{\mathbf{G}}$	flux vector in η transformed coordinate direction
H	total enthalpy per unit mass
$\widehat{\mathbf{H}}$	flux vector in ζ transformed coordinate direction
$\widehat{\mathbf{H}}_v$	viscous flux vector in ζ transformed coordinate direction
$\mathbf{I}$	identity matrix
i, j, k	index in ξ, η, and ζ transformed coordinate direction, respectively
$\widehat{i}, \widehat{j}, \widehat{k}$	unit vector in x, y, and z physical coordinate direction, respectively
J	Jacobian of transformation from physical coordinate system to computational coordinate system
L	lift
l	reference length, length of model from nose to end of solid jet plume simulator
ℓ	length of model from nose to juncture of nozzle exit and solid jet plume simulator
M_∞	free-stream Mach number
n	number of time steps
p	pressure
$\mathbf{Q}$	vector of dependent flow variables
$\widehat{\mathbf{Q}}$	transformed vector of dependent flow variables
q	square of velocity (see eqs. (3))
$\mathbf{q}$	vector of primitive variables
q_∞	free-stream dynamic pressure, $\frac{1}{2}\rho_\infty(u_\infty^2 + v_\infty^2 + w_\infty^2)$
$\mathbf{R}$	residual vector

R_ℓ	Reynolds number based on length of model from nose to nozzle exit
$\mathbf{S}$	directed surface area of cell face
$\mathbf{T}$	diagonalizing matrix
t	time
U	contravariant velocity component in ξ transformed direction
u	normalized x velocity component in physical coordinate system
V	contravariant velocity component in η transformed direction
v	normalized y velocity component in physical coordinate system
v	volume
W	contravariant velocity component in ζ transformed direction
w	normalized z velocity component in physical coordinate system
x	axial physical (Cartesian) coordinate, origin at nose of model
y	horizontal physical (Cartesian) coordinate, origin at nose of model
z	vertical physical (Cartesian) coordinate, origin at nose of model
β	exponent (see fig. 4(c))
γ	ratio of specific heats
Δ	incremental quantity or forward difference formula
Δt	incremental time
$\delta_\xi, \delta_\eta, \delta_\zeta$	differencing operator in ξ, η, and ζ direction, respectively (see for example eq. (13))
ζ	radial coordinate in transformed coordinate system
η	circumferential coordinate in transformed coordinate system
θ	circumferential coordinate, radians
κ	spatial differencing parameter (eq. (23))
κ_e	effective conductivity
μ	viscosity
ξ	axial coordinate in transformed coordinate system
ρ	density
σ	laminar Prandtl number
σ_t	turbulent Prandtl number
τ_w	local skin friction at wall
∇	backward difference formula

Subscripts:

c	corner dimension (fig. 4(c))
e	effective
i, j, k	index of cell location in ξ, η, and ζ transformed coordinate direction, respectively
L	left
n	nozzle (see fig. 4)
R	right
t	turbulent
∞	free-stream conditions

A boldface symbol denotes a vector quantity or a matrix; a tilde ($\tilde{}$) over a symbol denotes a Roe-averaged quantity; a caret ($\hat{}$) over a symbol denotes a transformed quantity; the superscript T denotes a transposed matrix.

Unless otherwise noted, all variables are nondimensionalized by appropriate combinations of the free-stream parameters and a reference length of 1 inch.

Computational Procedure

The three-dimensional Navier-Stokes numerical solution procedure used is described in references 10 through 13. In the procedure, the three-dimensional, time-dependent, Reynolds-averaged Navier-Stokes equations are written in strong conservation form. A thin layer assumption is made to simplify the dissipation terms. The turbulent contribution to these terms is simulated with the Baldwin-Lomax turbulence model (ref. 14).

The solution procedure employs the finite-volume principle where the spatial derivatives in the equations are evaluated as conservative flux balances across the grid cells. The fluxes at the cell interfaces are determined with upwind-biased flux-difference splitting in combination with a gradient limiting procedure to ensure monotonicity across discontinuities such as shock waves. The scheme is spatially third-order accurate. The time differencing algorithm used in the computational procedure is an approximately factored alternating-direction-implicit scheme in delta form. For completeness, a detailed

description of the computational procedure, including equations, used in this paper is presented in the appendix.

Computational Domain and Grid

A sketch of the three-dimensional computational domain illustrating the domain boundaries, grid topology, and model is presented in figure 1. To minimize computer run time and storage requirements, symmetry is assumed about the vertical plane, and only one half of the cylindrical domain is computed. The computational grid is body fitted (grid lines coincide with nacelle surface and other boundaries) in order to facilitate implementation of the boundary conditions.

The transverse, or cross-flow, planes of the three-dimensional coordinate system are generated by using the Thompson-Thames-Mastin elliptic method of reference 15. To construct the three-dimensional system, a series of these two-dimensional grids are positioned normal to an axis which is nominally aligned with the free-stream flow direction. This method of construction results in a sheared, H-type grid topology in the longitudinal planes, and an O-type topology in the cross-flow planes. (See fig. 1.)

The spacing of the mesh is stretched away from the model, with grid lines being radially clustered near the body surface and axially clustered on the afterbody. The spacing normal to the model surface is illustrated in figure 1. Figure 2 presents a wire-frame sketch of the model showing a typical grid spacing on its surface for a coarse mesh. The forebody, afterbody, and plume simulator are also defined in the figure.

Calculations were made with two computational meshes of different densities. The first grid system consisted of 64 grid planes in the axial direction (15 on the afterbody), 32 in the radial direction, and 10 in the circumferential direction. To assess the effects of grid refinement, calculations were also made with a mesh having 129 planes in the axial direction (29 on the afterbody), 65 in the radial direction, and 33 in the circumferential direction. For both meshes, the first radial grid point off the model surface is located 0.00076 inch from the surface. Based on the length of the model from the nose to the nozzle exit (approximately 63.25 inches), this amounts to 0.000012 of the model length. Most of the results presented were computed on the finer mesh.

Experimental Apparatus and Procedure

The experimental portion of this investigation was conducted in the Langley 16-Foot Transonic Wind Tunnel which is a continuous, atmospheric, single-return wind tunnel with an octagonal, slotted test section. A thorough descripton of the wind tunnel can be found in reference 16. The data presented are part of a broad experimental data base which was obtained for a nonaxisymmetric variable-geometry nozzle. The nozzle is typical of those currently advocated for advanced fighter airplanes. The parts of the data base that have already been published can be found in references 17 and 18.

For testing, the nozzle was mounted on a generic forebody which was supported in the wind tunnel by a sting-strut arrangement. Figure 3 shows a photograph of the model mounted in the wind tunnel. Details of the forebody and mounting system can be found in reference 17. Surface pressures on the nozzle were measured at free-stream Mach numbers up to 1.3. High pressure air was used to simulate the jet exhaust over a range of nozzle pressure ratios. During the investigation, Reynolds numbers based on the overall model length of 63.3 inches ranged from 17.2×10^6 at a free-stream Mach number of 0.60 to 29.3×10^6 at a free-stream Mach number of 0.94.

The specific nozzle configuration considered in this investigation represents a transonic-cruise, dry-power setting of the variable-geometry nozzle. Figure 4 presents a sketch of the configuration and gives its pertinent dimensions. Externally, the configuration is 7.24 inches long, 6.20 inches high, and 6.80 inches wide. At each longitudinal station, it has straight external sides with superelliptic corners. Both the external sidewall centerline and flap centerline are composed of circular arcs tangent to a straight section (refer to figs. 2, 3, and 4), with the circular-arc radii equal to 10.86 inches. The sidewall boattail angle is 6.93°, and the flap boattail angle is 17.56°. Internally, the sidewalls are flat. The nozzle has a throat area of 2.57 inch^2, a throat aspect ratio of 2.38, and an exit aspect ratio of 1.91. Its expansion ratio is 1.25 which yields a total pressure ratio for perfect expansion of approximately 4, the pressure ratio used for comparison with the computations.

Results and Discussion

Navier-Stokes solutions were obtained for the nonaxisymmetric afterbody at free-stream Mach numbers of 0.60, 0.80, and 0.94 and an angle of attack of 0°. To obtain the solutions, the afterbody was coupled with a forebody; thus, a complete model was created which matched the wind-tunnel configuration. The Reynolds numbers corresponding to the three free-stream Mach numbers were, respectively, 17.2×10^6, 19.5×10^6, and 29.3×10^6 based on the model length. All calculations were made with the three-dimensional Navier-Stokes procedure described

previously. In the experimental portion of the investigation, pressures were measured on the model afterbody. The computed pressure coefficients are compared with the wind-tunnel data.

Validity of the Solutions

Numerical convergence. In order to help assess the validity of the solutions, the numerical convergence characteristics were monitored as the solutions progressed in time. Figures 5 and 6 present the convergence history and the general features of the flow for solutions at free-stream Mach numbers of 0.60 and 0.80. At a Mach number of 0.60 (fig. 5(a)), the residual drops approximately four orders of magnitude in 1000 time steps. The drag coefficient reaches a constant value in approximately 400 time steps. The lift coefficient is zero throughout its time history since the computations are made at an angle of attack of 0°. These three histories indicate that the solution is converging and that it has essentially reached a steady state in about 400 time steps.

Figure 5(b) shows the computed pressure coefficient distributions along the top and side of the complete body. Comparing them with wind-tunnel data included in the figure shows that the calculated pressures along the entire length of the nacelle surface are reasonable. They agree well with the experimental data except at the compression peak near the juncture of the afterbody and the solid jet plume simulator. This discrepancy is discussed more fully later.

Figure 6 presents the convergence history and the solution at a Mach number of 0.80. The residual drops several orders of magnitude to a plateau where it oscillates with a small amplitude about a constant value. The plateau effect is thought to be a result of the discontinuous derivative of the min mod flux limiter in certain regions of the flow (ref. 11). There is good correlation between the computed pressures and wind-tunnel data over most of the nacelle. Again the exception to the good correlation is at the juncture of the afterbody and the plume simulator.

Grid convergence. A brief study of the effect of grid resolution on the quality of the solution was made in order to further assess the validity of the solution. In making this study, calculations were made with two computational meshes of different densities. The coarser mesh consisted of 64 grid planes in the axial direction (15 on the afterbody), 32 in the radial direction, and 10 in the circumferential direction. The finer mesh had 129 planes in the axial direction (29 on the afterbody), 65 in the radial direction, and 33 in the circumferential direction. Figure 7 presents the pressure distributions along the top and side of the afterbody and the cross-plane pressure distributions at the nozzle exit for both calculations. Both solutions agree well with the experimental data on the top and side rows except near the exit (figs. 7(a) and 7(b)). Although using the finer grid results in slightly better resolution for the top row, a comparison of the two solutions shows that grid resolution is not an issue on the top and side rows. The cross-plane pressure distributions at the exit (presented in fig. 7(c)), however, show that a fine grid is required if the solution is to be adequately resolved at the corners of the nonaxisymmetric nozzle.

The residual histories presented at free-stream Mach numbers of 0.60 and 0.80 (figs. 5 and 6) indicate that the solutions are converging numerically. The pressures at these Mach numbers look reasonable in all regions of the flow and agree well with the wind-tunnel values in regions where experimental data were obtained except near the exit. Furthermore, the solutions appear to be grid converged for the vertical and horizontal planes containing the model axis. Thus, within the constraints of the mathematical modeling of the physics, the solutions in the vertical and horizontal longitudinal planes seem to be converged to reasonably accurate representations of the true time-averaged flows being calculated.

Overall Solution Features and Comparison With Experiment

Figures 8 through 10 present details of the solutions for the three free-stream test Mach numbers. The details are specifically aimed at the afterbody region. The figures present Mach number contours, pressure distributions, and skin friction distributions for the top and side longitudinal planes or rows as the case may be. The Mach number contours are shown in parts (a) and (b) of the figures, the pressures in parts (c) and (d), and the skin friction distributions in parts (e) and (f).

$M_\infty = 0.60$. At a free-stream Mach number of 0.60, presented in figure 8, the flow is relatively mild with no shocks or separated regions present. The general structure of the flow field can be seen by looking at the local Mach number contours for the top and side longitudinal planes, shown in parts (a) and (b) of the figure. In particular, one can see the thinning of the boundary layer where the flow accelerates around the shoulder of the boattail and its corresponding thickening at the nozzle exit where the boattail ends and the solid jet plume simulator begins. The boundary-layer effects are more prominent along the top of the nozzle than they are on the side of the nozzle. This characteristic of the flow is to be expected since the boattail angle is much greater on

the top and bottom of the nozzle than on its sides. The larger angles result in greater accelerations of the flow accompanied by more severe changes in the boundary layer.

The pressure distributions shown in figures 8(c) and (d) reflect the structure of the flow indicated by the Mach number contours. They also correlate well with the wind-tunnel data over most of the nozzle boattail. A comparison of the calculated pressures and the data shows that the computations capture the level of the suction pressure peak exceptionally well. This good correlation occurs on both the top and side of the nozzle.

The one exception to the good correlation is at the juncture of the nozzle exit and the solid jet exhaust plume simulator. The discrepancy at the juncture is thought to be predominantly caused by the solid plume simulator inadequately modeling the jet exhaust plume. These results reiterate the well-established fact that the jet exhaust must be correctly modeled in order to accurately predict the flow near the nozzle exit. (See refs. 19 through 23, for example.) Not only does the solid plume simulator inaccurately model the shape of the jet exhaust plume, but it also fails to account for any entrainment of the afterbody flow by the jet exhaust.

The importance of accurately simulating both the blockage effects of the jet exhaust plume on external flow and the entrainment produced by the jet exhaust was experimentally demonstrated in references 19 and 20. In reference 21, entrainment was accounted for with some success when using solid jet plume simulators by reducing the size of the simulator. However, the size of the simulator needed for best results depended on the flow conditions. In references 22 and 23, the viscous-inviscid interaction computational procedure developed to simulate jet entrainment gave good predictions for flows with weak interactions. However, in the general case, the most accurate way to account for all the effects of the jet exhaust would be to include the exhaust in the Navier-Stokes calculations as was done in reference 9.

Another factor which may contribute to the calculated pressures being higher than the data is the inability of the turbulence model to predict the dissipation in the region of severe curvature at the juncture of the nozzle and simulator. (See refs. 24 and 25.) This factor is considered minor in this case though.

The calculated skin friction distributions are presented in figures 8(e) and (f). No experimental skin friction data exist for the afterbody. The skin friction levels seem to be reasonable and correlate with the pressure distributions.

$M_\infty = 0.80$. The solution at a free-stream Mach number of 0.80 is presented in figure 9. At this Mach number, the flow field has the same general structure as it does at a Mach number of 0.60, but the gradients and general features of the flow are magnified. A look at the pressure distributions presented in figure 9(c) shows that at a free-stream Mach number of 0.80, the flow goes slightly supersonic as it expands around the shoulder on top of the afterbody. Even under these conditions, the computations capture the negative pressure peak at the boattail shoulder exceptionally well for both the top and side of the nozzle. The skin friction predictions look reasonable at this Mach number also.

Again, as expected, the flow is not predicted well at the juncture of the nozzle and the solid plume simulator. The same comments concerning the inaccurate simulation of the jet plume apply at this Mach number as at Mach 0.60. Hence, the results give strong motivation to include the jet exhaust and its interaction with the external flow in the Navier-Stokes calculations.

$M_\infty = 0.94$. The results of the computations at a free-stream Mach number of 0.94 are presented in figure 10. At this Mach number, the solution procedure predicts large supersonic regions of flow. A shock exists on the top of the nozzle boattail and either a very weak shock or a strong compression exists on its side as can be seen from parts (a) and (b) of the figure. A much greater thinning of the boundary layer can be seen as the flow accelerates around the boattail shoulder than can be seen at the two lower Mach numbers. In addition, the predicted thickening of the boundary layer as the flow recompresses is much more dramatic than was found at the two lower Mach numbers.

Unfortunately, a comparison of the calculated pressures and the experimental data shows that the predicted flow over most of the top of the nozzle is only qualitatively correct in a very general sense. The measured wind-tunnel pressures show that the shock on top of the nozzle occurs much farther upstream than is predicted. Also, the data indicate that a large area on top of the nozzle aft of the shock is separated with a pressure plateau in the seperated region. The calculated pressures contain no significant pressure plateau and, thus, by themselves indicate no separation aft of the shock. The computed pressure recovery in this region is also much too large.

Improper simulation of entrainment undoubtedly has some role in overpredicting the pressure recovery in this case. However, the predominant reason for the poor prediction of the flow at this Mach number is attributed to the use of an algebraic eddy viscosity

turbulence model. (See refs. 24 and 25.) Reynolds-averaged Navier-Stokes calculations using eddy viscosity turbulence models typically predict the shock-wave too far downstream in transonic flows. They also commonly fail to give a significant plateau in the separated region. Some researchers have used relaxation equations for the eddy viscosity and achieved plateaus (for example, ref. 5). However, the results depended on the relaxation length, and the optimum length often depends on the flow. (See ref. 24 for a discussion of these points.) Hence, other classes of turbulence models need to be investigated for calculating transonic propulsion integration effects for fighter-type configurations.

Flow-Field Vortices

Formation and structure. Computed afterbody pressures along the top and side rows of the afterbody are compared in figure 11 for the turbulent solution at a free-stream Mach number of 0.80. In the expansion region, the pressures on top of the afterbody are considerably lower than the pressures on its side. Conversely, over the last part of the boattail, the recompression region, the pressures on the top are higher.

The impact of the circumferential variation of the pressures on the overall flow pattern is indicated in figure 12. The figure presents computed particle traces for the grid cells immediately next to the afterbody surface. Particle traces such as these give a picture of the flow patterns just off the surface and hence can be considered the numerical equivalent of experimental oil flows. An examination of the traces shows that the initially higher pressures on the side of the afterbody cause the flow to sweep from the sides, around the corners, and toward the center of the top of the afterbody. As the flow approaches the exit, the reversal of the circumferential location of the high and low pressures changes the direction of the sweep of the flow.

This swirling behavior of the flow suggests that vortices are likely to be generated. In order to determine if vortices exist, consider the cross-flow velocity vectors at several axial stations along the afterbody and downstream of the exit. Plots of these vectors are presented in figure 13. They show that at the beginning of the boattail, part (a) of the figure, the streamlines are mainly in the axial direction. Farther down the afterbody, strong inward radial velocities are created. Also, the flow begins to sweep from the sides of the afterbody, around the corners, and toward the centerline of the top and bottom of the afterbody in the manner indicated by the particle traces. At the nozzle exit, part (d), the suggestion of vortices at the corners of the nozzle can be seen.

At stations aft of the exit, the vortices become well formed and appear to move slightly outward as the flow progresses downstream. Finally, about $1\frac{1}{2}$ nozzle lengths aft of the exit, they appear to be getting larger in size and much less distinct which indicates that they are dissipating. In addition, at this point, the radial velocities have diminished in magnitude and changed direction from inward to outward.

Thus, the numerical solution technique predicts the formation and demise of vortices in the vicinity of the nonaxisymmetric nozzle. The existence of vortices behind this nonaxisymmetric nozzle was also discovered in the experimental investigation of reference 18.

Significance of vortices. The generation of vortices behind this nonaxisymmetric nozzle suggests that excessive drag is being created. Possibly, an afterbody with equal pressures on the sides and top and bottom where the flow does not tend to sweep around the corners would generate either weaker vortices or no vortices at all and hence have less drag. This idea is experimentally corroborated by the results of reference 26. During that experimental investigation, it was found that a nonaxisymmetric nozzle with equal boattail angles on the sides and top and bottom had less drag than the other nonaxisymmetric nozzles tested.

Computer Resources Required

The three-dimensional Navier-Stokes numerical solution technique takes approximately 75 microseconds per grid point per time step on the CYBER VPS 32 computer. This amounted to approximately 7.8 hours of computer time to get a steady-state solution on the refined grid. While this may seem like a large amount of computer time, the solutions yield a large amount of information about the complete flow field as has been demonstrated.

Concluding Remarks

The performance of a three-dimensional Navier-Stokes solution technique in predicting the transonic flow past a nonaxisymmetric nozzle has been investigated. The investigation was conducted at free-stream Mach numbers ranging from 0.60 to 0.94 and an angle of attack of 0°. Wind-tunnel data with the jet exhaust simulated with high pressure air were also obtained to compare with the numerical calculations. In the numerical procedure, the jet exhaust is represented by a solid sting.

The numerical solution procedure employs the three-dimensional, unsteady, Reynolds-averaged Navier-Stokes equations written in strong conservation form, a thin layer assumption, and the Baldwin-Lomax turbulence model. The equations are solved by using the finite-volume principle in conjunction with an approximately factored upwind-biased numerical algorithm.

The numerical experiments demonstrate that at the free-stream Mach numbers of 0.60 and 0.80, the Navier-Stokes solution technique predicts the flow over most of the afterbody quite well when no separation is present. At these Mach numbers, the solution technique does a particularly good job of capturing the negative pressure peak as the flow expands around the boattail shoulder.

The Navier-Stokes technique also successfully predicts the generation of vortices by the nonaxisymmetric afterbody, a phenomenon which has been experimentally verified. This successful prediction sheds insight into possible ways to reduce the afterbody drag and, thus, illustrates the potential usefulness of numerical techniques in solving propulsion-integration problems.

As expected, the procedure does not predict the flow well at the juncture of the nozzle exit and the solid jet plume simulator. This result reiterates the well-established fact that a solid plume simulator does not adequately represent the jet exhaust. Hence, it gives strong motivation to include the exhaust in the Navier-Stokes calculations. The numerical procedure also does not predict the flow well at the free-stream Mach number of 0.94 where there are strong shocks and large separated areas on the nozzle. Since algebraic eddy-viscosity turbulence models generally fail for this category of fluid flows, the suitability of other classes of turbulence models for calculating transonic afterbody flows needs to be investigated.

Nevertheless, considering all the results above, the three-dimensional Navier-Stokes numerical technique in its present form is a very useful research tool. Combining the use of the solution technique with the use of the wind tunnel to investigate transonic afterbody flows should yield new insights into the physics involved in these flows.

NASA Langley Research Center
Hampton, VA 23665-5225
April 28, 1989

Appendix

Computational Procedure

Governing Equations

The basic mathematical model of the physical laws governing the motion of a compressible fluid with dissipation is the set of Navier-Stokes equations. In the solution procedure used in this investigation, the three-dimensional, time-dependent, Reynolds-averaged Navier-Stokes equations are normalized and written in strong conservation form for a Cartesian coordinate system (x, y, z). Body forces play an insignificant role in the afterbody flow problem and are neglected. Since the dominant dissipative effects for the problem arise mainly from diffusion normal to the afterbody surface, a thin-layer assumption is made by retaining only those diffusion terms which are normal to the body surface. The resulting time-dependent equations for conservation of mass, linear momentum, and energy can then be expressed in terms of a fixed generalized coordinate system (ξ, η, ζ) as

$$\frac{\partial}{\partial t}\left(\hat{\mathbf{Q}}\right) + \frac{\partial}{\partial \xi}\left(\hat{\mathbf{F}}\right) + \frac{\partial}{\partial \eta}\left(\hat{\mathbf{G}}\right) + \frac{\partial}{\partial \zeta}\left(\hat{\mathbf{H}} - \hat{\mathbf{H}}_v\right) = 0 \tag{1}$$

where

$$\hat{\mathbf{Q}} = \frac{\mathbf{Q}}{J} = \frac{1}{J}\begin{Bmatrix} \rho \\ \rho u \\ \rho v \\ \rho w \\ e \end{Bmatrix} \tag{2a}$$

$$\hat{\mathbf{F}} = \frac{1}{J}\begin{Bmatrix} \rho U \\ \rho U u + \xi_x p \\ \rho U v + \xi_y p \\ \rho U w + \xi_z p \\ (e+p)U \end{Bmatrix} \tag{2b}$$

$$\hat{\mathbf{G}} = \frac{1}{J}\begin{Bmatrix} \rho V \\ \rho V u + \eta_x p \\ \rho V v + \eta_y p \\ \rho V w + \eta_z p \\ (e+p)V \end{Bmatrix} \tag{2c}$$

$$\hat{\mathbf{H}} = \frac{1}{J}\begin{Bmatrix} \rho W \\ \rho W u + \zeta_x p \\ \rho W v + \zeta_y p \\ \rho W w + \zeta_z p \\ (e+p)W \end{Bmatrix} \tag{2d}$$

$$\hat{\mathbf{H}}_v = \frac{M_\infty}{R_\ell}\frac{\mu_e}{J}\begin{Bmatrix} 0 \\ \phi_1 u_\zeta + \zeta_x \phi_2 \\ \phi_1 v_\zeta + \zeta_y \phi_2 \\ \phi_1 w_\zeta + \zeta_z \phi_2 \\ \phi_1 \left(\frac{q^2}{2}\right)_\zeta + \frac{1}{c_p}\frac{\kappa_e}{\mu_e}\frac{1}{(\gamma-1)}\left(c^2\right)_\zeta + W\phi_2 \end{Bmatrix} \tag{2e}$$

In these equations u, v, and w are velocity components in the physical coordinate system (x, y, z), ρ is the density, p is the pressure, c_p is the specific heat at constant pressure, and e is the total energy per unit volume. The terms μ_e and κ_e are, respectively, the effective viscosity and the effective conductivity which are composed of laminar and turbulent elements. Also,

$$\left.\begin{aligned} \phi_1 &= \zeta_x^2 + \zeta_y^2 + \zeta_z^2 \\ \phi_2 &= \frac{1}{3}\left(\zeta_x u_\zeta + \zeta_y v_\zeta + \zeta_z w_\zeta\right) \\ q^2 &= u^2 + v^2 + w^2 \\ R_\ell &= \frac{\rho_\infty q_\infty \ell}{\mu_\infty} \end{aligned}\right\} \tag{3}$$

The term ℓ is the reference length for determining the Reynolds number. In this paper, it is the length of the model from the nose to the exit (i.e., from the nose to the juncture of the nozzle and the solid jet plume simulator (fig. 2)).

The contravariant velocity components used in equations (2) are defined as

$$\left.\begin{aligned} U &= \xi_x u + \xi_y v + \xi_z w \\ V &= \eta_x u + \eta_y v + \eta_z w \\ W &= \zeta_x u + \zeta_y v + \zeta_z w \end{aligned}\right\} \tag{4}$$

and the metrics of the transformation as

$$\left.\begin{aligned}
\xi_x &= J(y_\eta z_\zeta - y_\zeta z_\eta) \\
\eta_x &= J(y_\zeta z_\xi - y_\xi z_\zeta) \\
\zeta_x &= J(y_\xi z_\eta - y_\eta z_\xi) \\
\xi_y &= J(x_\zeta z_\eta - x_\eta z_\zeta) \\
\eta_y &= J(x_\xi z_\zeta - x_\zeta z_\xi) \\
\zeta_y &= J(x_\eta z_\xi - x_\xi z_\eta) \\
\xi_z &= J(x_\eta y_\zeta - x_\zeta y_\eta) \\
\eta_z &= J(x_\zeta y_\xi - x_\xi y_\zeta) \\
\zeta_z &= J(x_\xi y_\eta - x_\eta y_\xi)
\end{aligned}\right\} \tag{5}$$

where J is the Jacobian of the transformation and is given by

$$J^{-1} = x_\xi(y_\eta z_\zeta - y_\zeta z_\eta) - y_\xi(x_\eta z_\zeta - x_\zeta z_\eta) + z_\xi(x_\eta y_\zeta - y_\eta x_\zeta) \tag{6}$$

Finally, the relations between the energy, pressure, and enthalpy for an ideal gas

$$\left.\begin{aligned}
p &= (\gamma - 1)\left(e - \frac{1}{2}\rho q^2\right) \\
\rho H &= \left(\frac{\gamma}{\gamma - 1}\right)p + \frac{1}{2}\rho q^2
\end{aligned}\right\} \tag{7}$$

complete the system of equations.

In the momentum equations, the effective viscosity μ_e is computed as

$$\mu_e = \mu + \mu_t = \mu\left(1 + \frac{\mu_t}{\mu}\right) \tag{8}$$

where μ is the molecular viscosity and μ_t is the turbulent viscosity. Similarly, in the energy equation, the effective conductivity κ_e is given by

$$\kappa_e = \kappa + \kappa_t = \frac{C_p}{\sigma}\mu + \frac{C_p}{\sigma_t}\mu_t = \frac{C_p\mu}{\sigma}\left(1 + \frac{\sigma}{\sigma_t}\frac{\mu_t}{\mu}\right) \tag{9}$$

where σ is the laminar Prandtl number and σ_t is the turbulent Prandtl number. The turbulence quantities are evaluated by using the algebraic eddy viscosity turbulence model of Baldwin and Lomax (ref. 14).

The governing equations are written here in a finite-difference form to facilitate describing the numerical algorithm. However, the equations are solved with the finite-volume technique or by summing the fluxes crossing the faces of each volume formed by the grid. Any appropriate pressure-area terms acting on the faces are added. The result is then equated to the time rate of change of the conserved quantity in each respective volume. In the finite-volume sense,

the state $\mathbf{Q}_{i,j,k}$ is not regarded as an approximation to the state at the cell center but as an approximation to the average state in the cell (ref. 27) or as

$$\mathbf{Q}^n_{i,j,k} = \frac{1}{\Delta \mathrm{v}} \int_{(i-\frac{1}{2})\Delta\xi,(j-\frac{1}{2})\Delta\eta,(k-\frac{1}{2})\Delta\zeta}^{(i+\frac{1}{2})\Delta\xi,(j+\frac{1}{2})\Delta\eta,(k+\frac{1}{2})\Delta\zeta} \mathbf{Q}(\xi, \eta, \zeta, n\Delta t)\, d\mathrm{v} \tag{10}$$

where $\Delta \mathrm{v}$ is the incremental volume, Δt the incremental time, and n denotes the time step. In the present formulations, the spacing in the transformed plane is unity; that is,

$$\left.\begin{aligned} \xi_{i+\frac{1}{2}} - \xi_{i-\frac{1}{2}} &= 1 \\ \eta_{j+\frac{1}{2}} - \eta_{j-\frac{1}{2}} &= 1 \\ \zeta_{k+\frac{1}{2}} - \zeta_{k-\frac{1}{2}} &= 1 \end{aligned}\right\} \tag{11}$$

The relationship between the finite-volume and finite-difference representations of the equations can be seen by comparing the discretized forms of each representation (ref. 28). Specifically, this comparison illustrates how the Jacobian and metric derivatives in the finite-difference formulation relate to the cell volume and cell face areas in the finite-volume formulation. For instance, because of equations (11),

$$\frac{1}{J} \equiv \text{Cell volume}$$

$$\frac{\xi_x}{J}, \frac{\xi_y}{J}, \frac{\xi_z}{J} \equiv x, y, z \text{ components of directed area of cell face perpendicular to } \xi = \text{Constant coordinate plane}$$

which gives

$$(\mathbf{S})_{i+\frac{1}{2}} = \frac{\xi_x}{J}\hat{i} + \frac{\xi_y}{J}\hat{j} + \frac{\xi_z}{J}\hat{k}$$

where $\hat{i}, \hat{j}, \hat{k}$ are the unit vectors in the x, y, z directions, the subscript i refers to the cell-centered location (i, j, k), $i + \frac{1}{2}$ corresponds to a cell interface location $(i + \frac{1}{2}, j, k)$, and $\mathbf{S}$ is the directed area of the cell face normal to the ξ coordinate.

Numerical Algorithm

Finite-volume solution procedure. Although references are made to differencing in the following discussion of the computational algorithm, it should be remembered that the actual operations are carried out by using the finite-volume method. In other words, the spatial derivatives shown in the equations are actually evaluated as a conservative flux balance across a cell. For example,

$$\begin{aligned} \left(\frac{\partial \hat{\mathbf{F}}}{\partial \xi}\right)_i &= \delta_\xi(\hat{\mathbf{F}}) = \hat{\mathbf{F}}_{i+\frac{1}{2}} - \hat{\mathbf{F}}_{i-\frac{1}{2}} \\ &= (\mathbf{S} \cdot \underline{\mathbf{F}})_{i+\frac{1}{2}} - (\mathbf{S} \cdot \underline{\mathbf{F}})_{i-\frac{1}{2}} \end{aligned} \tag{13}$$

where

$$\underline{\mathbf{F}} = \mathbf{F}\hat{i} + \mathbf{G}\hat{j} + \mathbf{H}\hat{k}$$

By approximating the equations in this manner, one discretizes the equations for the numerical solution procedure. The interface fluxes $\mathbf{S} \cdot \underline{\mathbf{F}}$ depicted in equation (13) are determined from the following characteristic-based method.

Interface flux. The convective and pressure terms at the cell interfaces are determined with the Roe type of upwind-biased flux-difference splitting of references 27 and 29. The method accounts for all different waves by which neighboring cells interact, including entropy and shear waves. In this method, the interface flux is written as the exact solution to an approximate Riemann problem

$$\hat{\mathbf{F}}_{i+\frac{1}{2}} = \frac{1}{2}\left[\hat{\mathbf{F}}(\mathbf{Q}_L) + \hat{\mathbf{F}}(\mathbf{Q}_R) - |\tilde{\mathbf{A}}|(\mathbf{Q}_R - \mathbf{Q}_L)\right]_{i+\frac{1}{2}} \tag{14}$$

where $\tilde{\mathbf{A}}$ is $\mathbf{A}$ evaluated at Roe-averaged variables defined subsequently. Hence,

$$|\tilde{\mathbf{A}}| = |\mathbf{A}(\tilde{\mathbf{Q}})|$$

and

$$\tilde{\mathbf{Q}} = \tilde{\mathbf{Q}}(\mathbf{Q}_L, \mathbf{Q}_R)$$

The variables $\mathbf{Q}_L$ and $\mathbf{Q}_R$ are the state variables to the left and right of the cell faces, and

$$\left.\begin{aligned} \mathbf{A} &= \frac{\partial \hat{\mathbf{F}}}{\partial \mathbf{Q}} = \mathbf{T}\boldsymbol{\Lambda}\mathbf{T}^{-1} = \mathbf{T}(\boldsymbol{\Lambda}^{+} + \boldsymbol{\Lambda}^{-})\mathbf{T}^{-1} \\ \boldsymbol{\Lambda}^{\pm} &= \frac{\boldsymbol{\Lambda} \pm |\boldsymbol{\Lambda}|}{2} \\ |\mathbf{A}| &= \mathbf{T}|\boldsymbol{\Lambda}|\mathbf{T}^{-1} \end{aligned}\right\} \tag{15}$$

The diagonal matrix $\boldsymbol{\Lambda}$ is the matrix of eigenvalues of $\mathbf{A}$, $\mathbf{T}$ is the matrix of right eigenvectors as columns, and $\mathbf{T}^{-1}$ the matrix of left eigenvectors as rows. They are all evaluated at Roe-averaged values such that

$$\hat{\mathbf{F}}(\mathbf{Q}_R) - \hat{\mathbf{F}}(\mathbf{Q}_L) = \tilde{\mathbf{A}}(\mathbf{Q}_R - \mathbf{Q}_L) \tag{16}$$

is satisfied exactly.

The third term in equation (14), $|\tilde{\mathbf{A}}|(\mathbf{Q}_R - \mathbf{Q}_L)$, can be written as

$$|\tilde{\mathbf{A}}|(\mathbf{Q}_R - \mathbf{Q}_L) \equiv |\tilde{\mathbf{A}}|\Delta\mathbf{Q}$$

$$= \begin{Bmatrix} \alpha_4 \\ \tilde{u}\alpha_4 + k_x\alpha_5 + \alpha_6 \\ \tilde{v}\alpha_4 + k_y\alpha_5 + \alpha_7 \\ \tilde{w}\alpha_4 + k_z\alpha_5 + \alpha_8 \\ \tilde{H}\alpha_4 + \tilde{\underline{u}}\alpha_5 + \tilde{u}\alpha_6 + \tilde{v}\alpha_7 + \tilde{w}\alpha_8 - \left(\frac{\tilde{c}^2}{\gamma - 1}\right)\alpha_1 \end{Bmatrix} \tag{17}$$

where

$$\left.\begin{aligned}
\alpha_1 &= \left|\frac{\operatorname{grad}\xi}{J}\right| |\tilde{\underline{u}}| \left(\Delta\rho - \frac{\Delta p}{\tilde{c}^2}\right) \\
\alpha_2 &= \frac{1}{2\tilde{c}^2}\left|\frac{\operatorname{grad}\xi}{J}\right| |\tilde{\underline{u}} + \tilde{c}| \left(\Delta p + \tilde{\rho}\tilde{c}\Delta\underline{u}\right) \\
\alpha_3 &= \frac{1}{2\tilde{c}^2}\left|\frac{\operatorname{grad}\xi}{J}\right| |\tilde{\underline{u}} - \tilde{c}| \left(\Delta p - \tilde{\rho}\tilde{c}\Delta\underline{u}\right) \\
\alpha_4 &= \alpha_1 + \alpha_2 + \alpha_3 \\
\alpha_5 &= \tilde{c}\left(\alpha_2 - \alpha_3\right) \\
\alpha_6 &= \left|\frac{\operatorname{grad}\xi}{J}\right| |\tilde{\underline{u}}| \left(\tilde{\rho}\Delta u - k_x\tilde{\rho}\Delta\underline{u}\right) \\
\alpha_7 &= \left|\frac{\operatorname{grad}\xi}{J}\right| |\tilde{\underline{u}}| \left(\tilde{\rho}\Delta v - k_y\tilde{\rho}\Delta\underline{u}\right) \\
\alpha_8 &= \left|\frac{\operatorname{grad}\xi}{J}\right| |\tilde{\underline{u}}| \left(\tilde{\rho}\Delta w - k_z\tilde{\rho}\Delta\underline{u}\right)
\end{aligned}\right\} \tag{18}$$

The notation $\tilde{}$ denotes the following Roe-averaged evaluations

$$\left.\begin{aligned}
\tilde{\rho} &= \sqrt{\rho_L\rho_R} \\
\tilde{u} &= \frac{u_L + u_R\sqrt{\rho_R/\rho_L}}{1 + \sqrt{\rho_R/\rho_L}} \\
\tilde{v} &= \frac{v_L + v_R\sqrt{\rho_R/\rho_L}}{1 + \sqrt{\rho_R/\rho_L}} \\
\tilde{w} &= \frac{w_L + w_R\sqrt{\rho_R/\rho_L}}{1 + \sqrt{\rho_R/\rho_L}} \\
\tilde{H} &= \frac{H_L + H_R\sqrt{\rho_R/\rho_L}}{1 + \sqrt{\rho_R/\rho_L}} \\
\tilde{c}^2 &= (\gamma - 1)\tilde{H} - \frac{\tilde{u}^2 + \tilde{v}^2 + \tilde{w}^2}{2}
\end{aligned}\right\} \tag{19}$$

In equations (19), the magnitude of the cell interface directed area is $\left|\frac{\text{grad}\,\xi}{J}\right|$ and the direction cosines are

$$(k_x, k_y, k_z) = \frac{(\xi_x, \xi_y, \xi_z)}{|\text{grad}\,\xi|} \tag{20}$$

where the normalized contravariant velocity component normal to the cell interface is denoted

$$\underline{u} = k_x u + k_y v + k_z w \tag{21}$$

State-variable interpolations. The state-variable interpolations determine the resulting accuracy of the scheme. The state variables at the interface are constructed from the primitive variables $\mathbf{q} = [\rho, u, v, w, p]^T$. The interpolation

$$\left.\begin{aligned} (\mathbf{q}_L)_{i+\frac{1}{2}} &= \mathbf{q}_i \\ (\mathbf{q}_R)_{i+\frac{1}{2}} &= \mathbf{q}_{i+1} \end{aligned}\right\} \tag{22}$$

corresponds to first-order fully upwind differencing. Higher order accuracy is given by the family of interpolations

$$\left.\begin{aligned} (\mathbf{q}_L)_{i+\frac{1}{2}} &= \mathbf{q}_i + \frac{1}{4}\left[(1-\kappa)\overline{\nabla \mathbf{q}}_i + (1+\kappa)\overline{\Delta \mathbf{q}}_i\right] \\ (\mathbf{q}_R)_{i+\frac{1}{2}} &= \mathbf{q}_{i+1} - \frac{1}{4}\left[(1+\kappa)\overline{\nabla \mathbf{q}}_{i+1} + (1-\kappa)\overline{\Delta \mathbf{q}}_{i+1}\right] \end{aligned}\right\} \tag{23}$$

where $\overline{\nabla \mathbf{q}}_i$ and $\overline{\Delta \mathbf{q}}_i$ are, respectively, backward and forward differences of $\mathbf{q}$. All the calculations presented were made with κ set to 1/3, a value which corresponds to a third-order accurate spatial discretization.

In order to ensure a monotone interpolation of $\mathbf{q}$ at the interfaces, the min mod flux limiter described in reference 11

$$\left.\begin{aligned} \overline{\nabla \mathbf{q}} &= \text{min mod}(\nabla \mathbf{q}, b\Delta \mathbf{q}) \\ \overline{\Delta \mathbf{q}} &= \text{min mod}(\Delta \mathbf{q}, b\nabla \mathbf{q}) \end{aligned}\right\} \tag{24}$$

was used where

$$\text{min mod}(x, y) = \max\{0, \min[x\ \text{sign}(y), by\ \text{sign}(x)]\}\ \text{sign}(x) \tag{25}$$

and

$$b = \frac{3-\kappa}{1-\kappa}$$

Time-differencing algorithm. The time-differencing algorithm used in the computational procedure is an approximately factored alternating-direction implicit scheme in delta form. Similar to the Beam and Warming technique of reference 30, equation (1) is factored and solved in the following steps:

$$\left.\begin{aligned}
\left[\frac{\mathbf{I}}{J\Delta t}+\delta_\xi\frac{\partial\hat{\mathbf{F}}}{\partial\mathbf{Q}}\right]\Delta\mathbf{Q}^{**} &= -\mathbf{R}^n \\
\left[\frac{\mathbf{I}}{J\Delta t}+\delta_\eta\frac{\partial\hat{\mathbf{G}}}{\partial\mathbf{Q}}\right]\Delta\mathbf{Q}^{*} &= \frac{\mathbf{I}}{J\Delta t}\Delta\mathbf{Q}^{**} \\
\left[\frac{\mathbf{I}}{J\Delta t}+\delta_\zeta\left(\frac{\partial\hat{\mathbf{H}}}{\partial\mathbf{Q}}-\frac{\partial\hat{\mathbf{H}}_v}{\partial\mathbf{Q}}\right)\right]\Delta\mathbf{Q} &= \frac{I}{J\Delta t}\Delta\mathbf{Q}^{*}
\end{aligned}\right\} \tag{26}$$

where $\Delta\mathbf{Q}$ is the difference in $\mathbf{Q}$ between time levels $n+1$ and n

$$\mathbf{Q}^{n+1}=\mathbf{Q}^n+\Delta\mathbf{Q} \tag{27}$$

and

$$\mathbf{R}^n=\delta_\xi\hat{\mathbf{F}}^n+\delta_\eta\hat{\mathbf{G}}^n+\delta_\zeta(\hat{\mathbf{H}}-\hat{\mathbf{H}}_v)^n \tag{28}$$

The right-hand, or explicit, side of equations (26) is computed by evaluating the fluxes at the cell interfaces with the third-order accurate upwind-biased discretization. In the implicit, or left-hand side of the equation, the fluxes are evaluated with the first-order-accurate upwind discretization.

The Jacobian matrices are evaluated explicitly. An example of their definition using the flux vector $\hat{\mathbf{F}}$ is

$$\frac{\partial\hat{\mathbf{F}}}{\partial\mathbf{Q}}=\frac{\partial\hat{\mathbf{F}}}{\partial\mathbf{Q}_L}\frac{\partial\mathbf{Q}_L}{\partial\mathbf{Q}}+\frac{\partial\hat{\mathbf{F}}}{\partial\mathbf{Q}_R}\frac{\partial\mathbf{Q}_R}{\partial\mathbf{Q}} \tag{29}$$

At a specific interface, $\partial\mathbf{Q}_L/\partial\mathbf{Q}$ and $\partial\mathbf{Q}_R/\partial\mathbf{Q}$ determine the proper cell from which to obtain $\mathbf{Q}$ in computing each term in equation (29). For instance, for the $i+\frac{1}{2}$ interface and using first-order-accurate upwind discretization, $\partial\mathbf{Q}_L/\partial\mathbf{Q}$ is equal to 1 for a cell centered at i and is 0 for all other locations. Futhermore, $\partial\mathbf{Q}_R/\partial\mathbf{Q}$ is 1 for a cell centered at $i+1$ and 0 for all other locations. Thus, at the $i+\frac{1}{2}$ interface, the first term in equation (29) becomes

$$\frac{\partial\hat{\mathbf{F}}_{i+\frac{1}{2}}}{\partial\mathbf{Q}_L}=\frac{\partial}{\partial\mathbf{Q}_L}\left\{\frac{1}{2}\left[\hat{\mathbf{F}}_L+\hat{\mathbf{F}}_R-|\tilde{\mathbf{A}}|(\mathbf{Q}_R-\mathbf{Q}_L)\right]_{i+\frac{1}{2}}\right\} \tag{30}$$

or

$$\frac{\partial\hat{\mathbf{F}}_{i+\frac{1}{2}}}{\partial\mathbf{Q}_L}=\frac{1}{2}\left[\mathbf{A}_L-\frac{\partial|\tilde{\mathbf{A}}|}{\partial\mathbf{Q}_L}(\mathbf{Q}_R-\mathbf{Q}_L)+|\tilde{\mathbf{A}}|_{i+\frac{1}{2}}\right] \tag{31}$$

The second term in equation (31) is very small and is neglected. Approximating the third term gives

$$\frac{\partial\hat{\mathbf{F}}_{i+\frac{1}{2}}}{\partial\mathbf{Q}_L}\approx\frac{1}{2}\left[\mathbf{A}_i+|\mathbf{A}|_i\right] \tag{32}$$

Similarly,

$$\frac{\partial\tilde{\mathbf{F}}_{i+\frac{1}{2}}}{\partial\mathbf{Q}_R}\approx\frac{1}{2}\left[\mathbf{A}_{i+1}-|\mathbf{A}|_{i+1}\right]$$

The Jacobian matrices for the flux at the $i-\frac{1}{2}$ interface are determined following the same general procedure.

Substituting values similar to these spatially first-order-accurate upwind discretizations into equations (26) results in a block-tridiagonal system of equations to be solved in each of the three directions. In the i direction, this system of equations takes the form

$$
\begin{aligned}
&-\mathbf{A}^{+}\left(\mathbf{Q}_{i-1},(\mathbf{S})_{i-\frac{1}{2}}\right)\Delta\mathbf{Q}_{i-1}^{**} \\
&+\left[\frac{\mathbf{I}}{(J\Delta t)_i}+\mathbf{A}^{+}\left(\mathbf{Q}_i,(\mathbf{S})_{i+\frac{1}{2}}\right)-\mathbf{A}^{-}\left(\mathbf{Q}_i,(\mathbf{S})_{i-\frac{1}{2}}\right)\right]\Delta\mathbf{Q}_i^{**} \\
&+\mathbf{A}^{-}\left(\mathbf{Q}_{i+1},(\mathbf{S})_{i+\frac{1}{2}}\right)\Delta\mathbf{Q}_{i+1}^{**}=-\mathbf{R}^{n}
\end{aligned}
\tag{33}
$$

where

$$\mathbf{A}^{+}=\frac{1}{2}\left[\mathbf{A}+|\mathbf{A}|\right]$$

$$\mathbf{A}^{-}=\frac{1}{2}\left[\mathbf{A}-|\mathbf{A}|\right]$$

Each system of equations is solved with a full 5- by 5-block-tridiagonal inversion procedure.

Boundary Conditions

At the body, the velocity normal to the surface is set to zero and no-slip conditions are imposed to yield $u=v=w=0$. An adiabatic wall condition is employed for temperature at the body. The pressure on the body surface is obtained by setting the normal pressure gradient equal to zero (a good assumption for viscous flow)and then extrapolating the pressure to the surface.

The other boundaries of the computational domain are the inflow boundary, the far-field boundary, the outflow boundary at the downstream end of the domain, the axis ahead of the body, and the symmetry boundaries. Figure 1 illustrates these boundaries. At the inflow boundary, the treatment is based on the Riemann invariants for one-dimensional flow normal to the boundary. This method of treating a boundary is discussed thoroughly in references 31 and 32. The same method of treatment is used at the far-field boundary where the flow at each individual point could be either into or out of the computational domain. At the downstream boundary, zeroth order extrapolation of all variables is used. Reflection conditions are used at the symmetry boundaries and on the axis.

References

1. Capone, Francis J.: The Nonaxisymmetric Nozzle—It Is for Real. AIAA Paper 79-1810, Aug. 1979.
2. Runckel, Jack F.: *Interference Between Exhaust System and Afterbody of Twin-Engine Fuselage Configurations.* NASA TN D-7525, 1974.
3. Shevell, Richard S.: Aerodynamic Bugs: Can CFD Spray Them Away? AIAA-85-4067, Oct. 1985.
4. Rubbert, Paul E.; and Tinoco, Edward N.: The Impact of Computational Aerodynamics on Aircraft Design. AIAA-83-2060, Aug. 1983.
5. Swanson, R. Charles, Jr.: *Numerical Solutions of the Navier-Stokes Equations for Transonic Afterbody Flows.* NASA TP-1784, 1980.
6. Swanson, R. C.: Navier-Stokes Solutions for Nonaxisymmetric Nozzle Flows. AIAA-81-1217, June 1981.
7. Deiwert, George S.: Supersonic Axisymmetric Flow Over Boattails Containing a Centered Propulsive Jet. *AIAA J.*, vol. 22, no. 10, Oct. 1984, pp. 1358–1365.
8. Deiwert, George S.; Andrews, Alison E.; and Nakahashi, Kazuhiro: Theoretical Analysis of Aircraft Afterbody Flow. *J. Spacecr. & Rockets*, vol. 24, no. 6, Nov.–Dec. 1987, pp. 496–503.
9. Deiwert, George S.; and Rothmund, Herbert: Three-Dimensional Flow Over a Conical Afterbody Containing a Centered Propulsive Jet: A Numerical Simulation. AIAA-83-1709, July 1983.
10. Thomas, James L.; and Newsome, Richard W.: Navier-Stokes Computations of Lee-Side Flows Over Delta Wings. AIAA-86-1049, May 1986.
11. Anderson, W. Kyle; Thomas, James L.; and Van Leer, Bram: A Comparison of Finite Volume Flux Vector Splittings for the Euler Equations. AIAA-85-0122, Jan. 1985.
12. Van Leer, Bram; Thomas, James L.; Roe, Philip L.; and Newsome, Richard W.: A Comparison of Numerical Flux Formulas for the Euler and Navier-Stokes Equations. *A Collection of Technical Papers—AIAA 8th Computational Fluid Dynamics Conference*, 1987, pp. 36–41. (Available as AIAA-87-1104.)
13. Vatsa, V. N.; Thomas, J. L.; and Wedan, B. W.: Navier-Stokes Computations of Prolate Spheroids at Angle of Attack. *A Collection of Technical Papers—AIAA Atmospheric Flight Mechanics Conference*, 1987, pp. 488–506. (Available as AIAA-87-2627.)
14. Baldwin, Barrett; and Lomax, Harvard: Thin-Layer Approximation and Algebraic Model for Separated Turbulent Flows. AIAA Paper 78-257, Jan. 1978.
15. Thompson, Joe F.; Thames, Frank C.; and Mastin, C. Wayne: *Boundary-Fitted Curvilinear Coordinate Systems for Solution of Partial Differential Equations on Fields Containing Any Number of Arbitrary Two-Dimensional Bodies.* NASA CR-2729, 1977.
16. Corson, Blake W., Jr.; Runckel, Jack F.; and Igoe, William B.: *Calibration of the Langley 16-Foot Transonic Tunnel With Test Section Air Removal.* NASA TR R-423, 1974.
17. Mason, Mary L.; and Abeyounis, William K.: *Experimental Investigation of Two Nonaxisymmetric Wedge Nozzles at Free-Stream Mach Numbers up to 1.20.* NASA TP-2054, 1982.
18. Putnam, Lawrence E.; and Mercer, Charles E.: *Pitot-Pressure Measurements in Flow Fields Behind a Rectangular Nozzle With Exhaust Jet for Free-Stream Mach Numbers of 0.00, 0.60, and 1.20.* NASA TM-88990, 1986.
19. Compton, William B., III: An Experimental Study of Jet Exhaust Simulation Parameters. M.S. Thesis, George Washington Univ., Aug. 1973.
20. Compton, William B., III: *Effects of Jet Exhaust Gas Properties on Exhaust Simulation and Afterbody Drag.* NASA TR R-444, 1975.
21. Reubush, David E.: *Experimental Study of the Effectiveness of Cylindrical Plume Simulators for Predicting Jet-On Boattail Drag at Mach Numbers up to 1.30.* NASA TN D-7795, 1974.
22. Wilmoth, R. G.; Dash, S. M.; and Pergament, H. S.: A Numerical Study of Jet Entrainment Effects on the Subsonic Flow Over Nozzle Afterbodies. AIAA Paper 79-0135, Jan. 1979.
23. Wilmoth, Richard G.: *Viscous-Inviscid Calculations of Jet Entrainment Effects on the Subsonic Flow Over Nozzle Afterbodies.* NASA TP-1626, 1980.
24. Marvin, Joseph G.: Turbulence Modeling for Computational Aerodynamics. *AIAA J.*, vol. 21, no. 7, July 1983, pp. 941–955.
25. Lakshminarayana, B.: Turbulence Modelling for Complex Shear Flows. AIAA-85-1652, July 1985.
26. Bangert, Linda S.; Leavitt, Laurence D.; and Reubush, David E.: *Effects of Afterbody Boattail Design and Empennage Arrangement on Aeropropulsive Characteristics of a Twin-Engine Fighter Model at Transonic Speeds.* NASA TP-2704, 1987.
27. Roe, P. L.: Characteristic-Based Schemes for the Euler Equations. *Annual Review of Fluid Mechanics*, Volume 18, Milton van Dyke, J. V. Wehausen, and John L. Lumley, eds., Annual Reviews Inc., 1986, pp. 337–365.
28. Gnoffo, Peter A.: A Vectorized, Finite-Volume, Adaptive-Grid Algorithm for Navier-Stokes Calculations. *Numerical Grid Generation*, Joe F. Thompson, ed., Elsevier Science Publ. Co., Inc., c.1982, pp. 819–835.
29. Roe, P. L.; and Pike, J.: Efficient Construction and Utilisation of Approximate Riemann Solutions. *Computing Methods in Applied Sciences and Engineering*, VI, R. Glowinski and J.-L. Lions, eds., Elsevier Science Publ. Co., Inc., 1984, pp. 499–518.
30. Beam, Richard M.; and Warming, R. F.: An Implicit Factored Scheme for the Compressible Navier-Stokes Equations. *AIAA J.*, vol. 16, no. 4, Apr. 1978, pp. 393–402.
31. Jameson, Antony; and Baker, Timothy J.: Solution of the Euler Equations for Complex Configurations. *A Collection of Technical Papers—AIAA 6th Computational Fluid Dynamics Conference*, 1983, pp. 293–302. (Available as AIAA-83-1929.)
32. Thomas, James L.; and Salas, M. D.: Far-Field Boundary Conditions for Transonic Lifting Solutions to the Euler Equations. AIAA-85-0020, Jan. 1985.

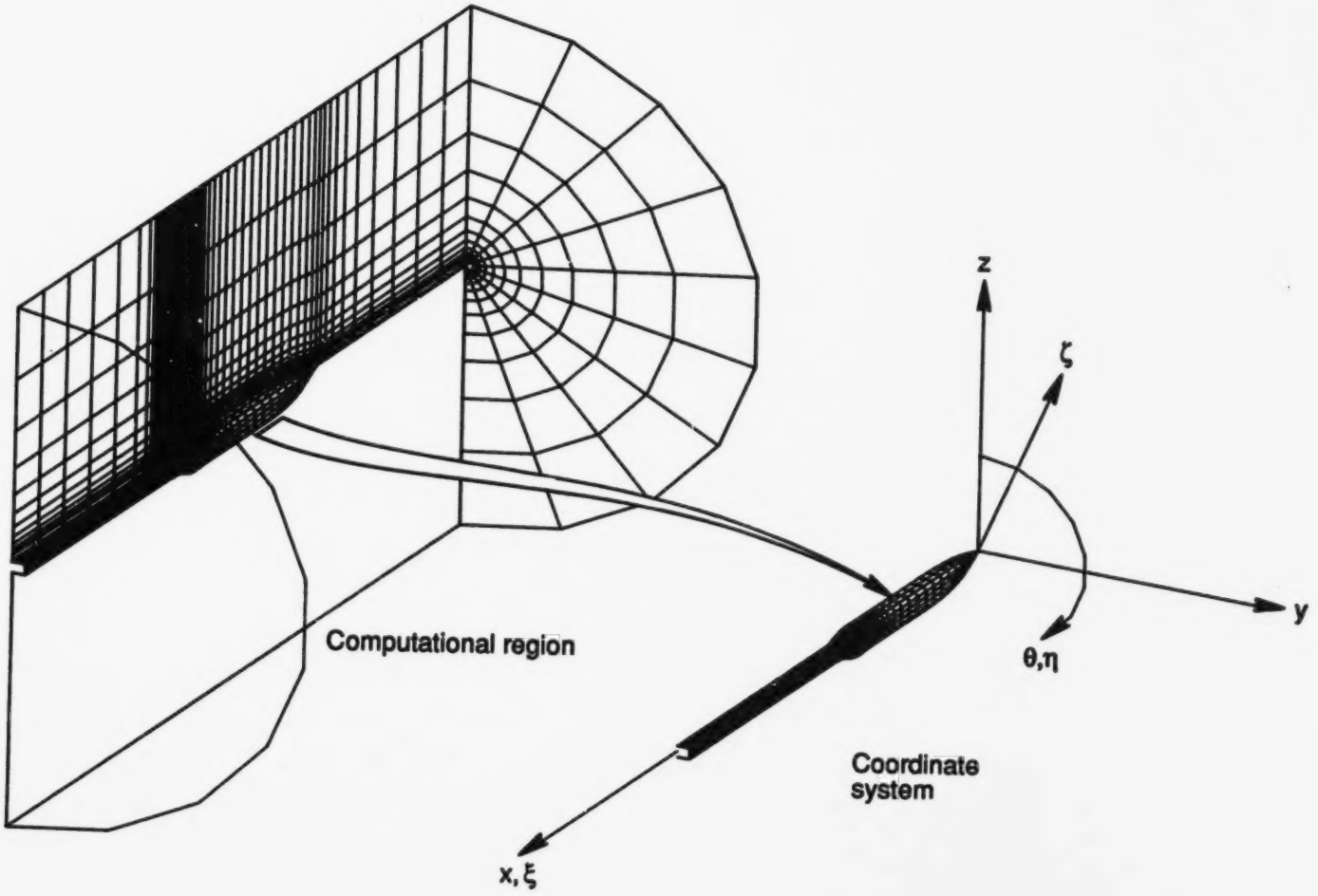

Figure 1. Three-dimensional computational region and grid.

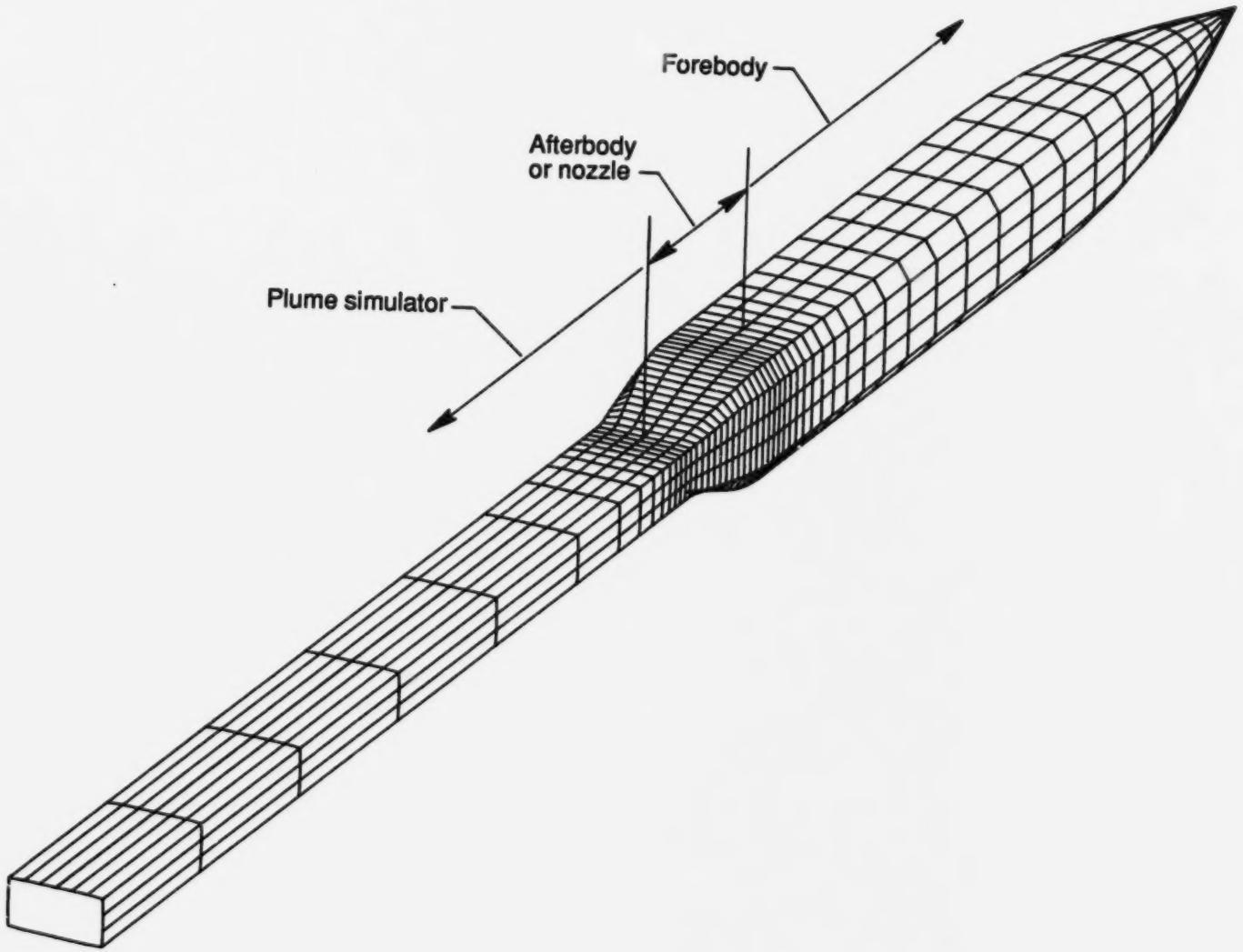

Figure 2. Nonaxisymmetric computational body with solid jet exhaust plume simulator.

ORIGINAL PAGE IS
OF POOR QUALITY

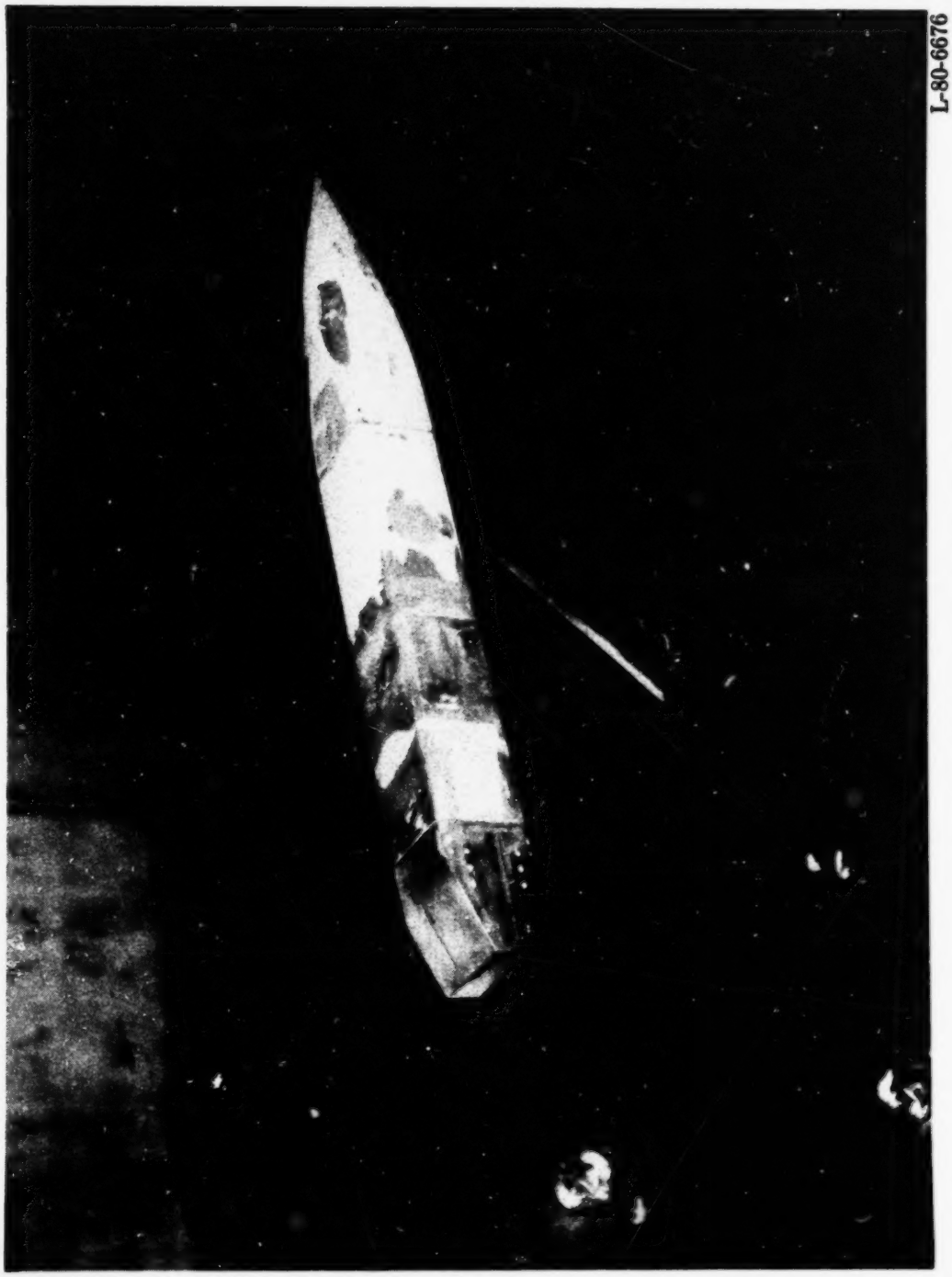

L-80-6676

Figure 3. Model mounted in wind tunnel.

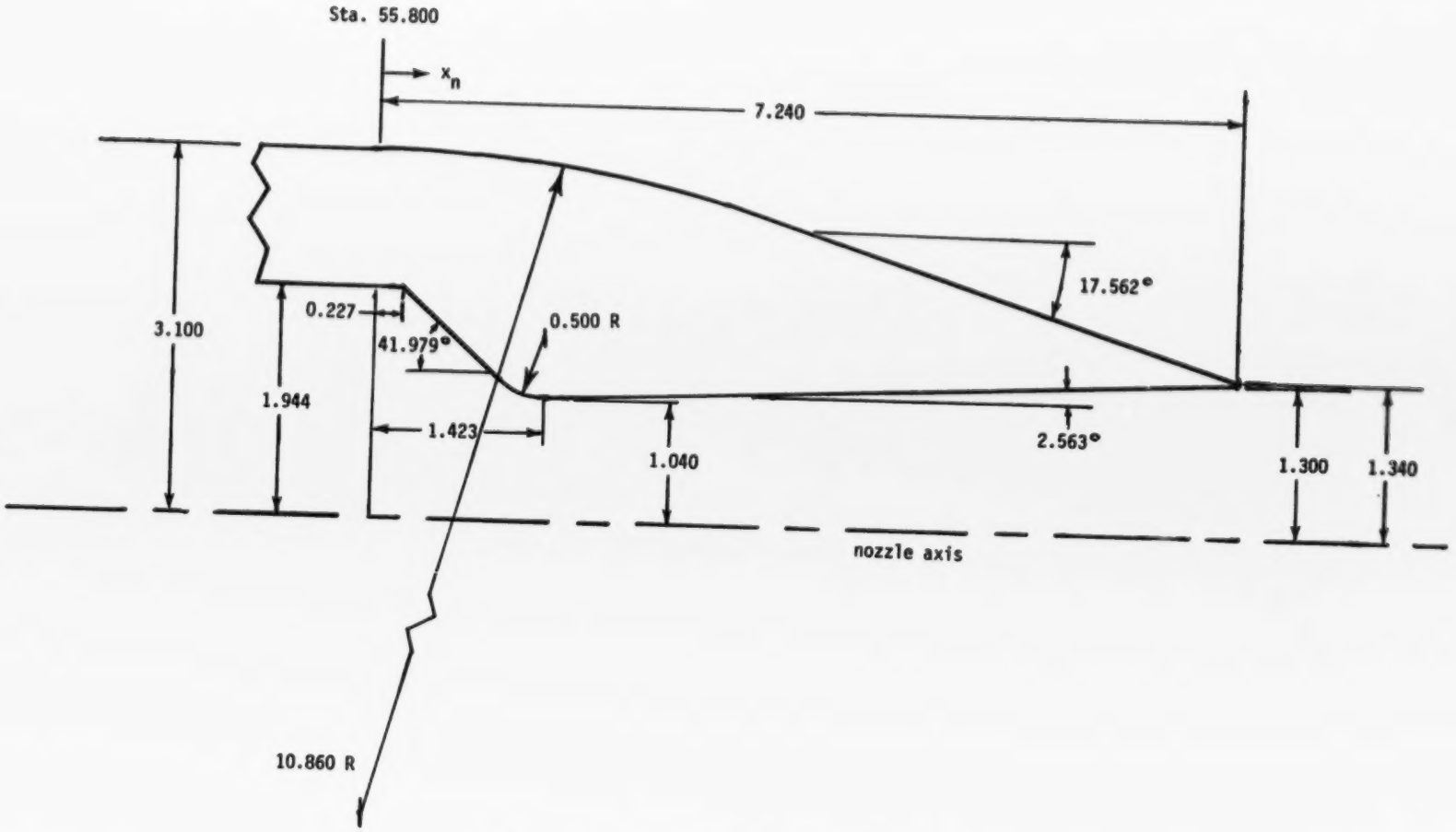

(a) Flap geometry (centerline cross section).

Figure 4. Nonaxisymmetric nozzle geometry. Transonic-cruise, dry-power configuration; all linear dimensions are in inches.

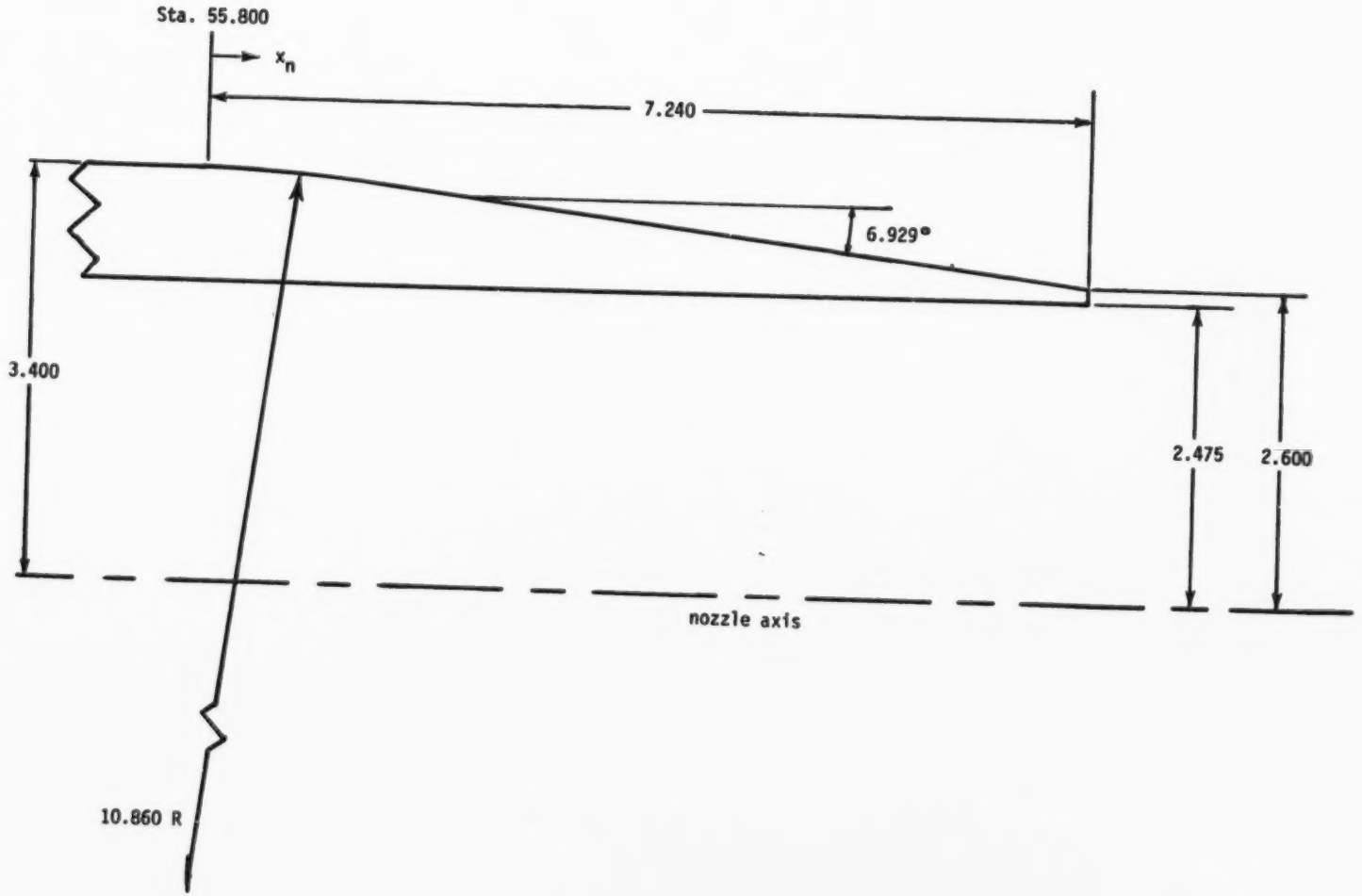

(b) Sidewall geometry (centerline cross section).

Figure 4. Continued.

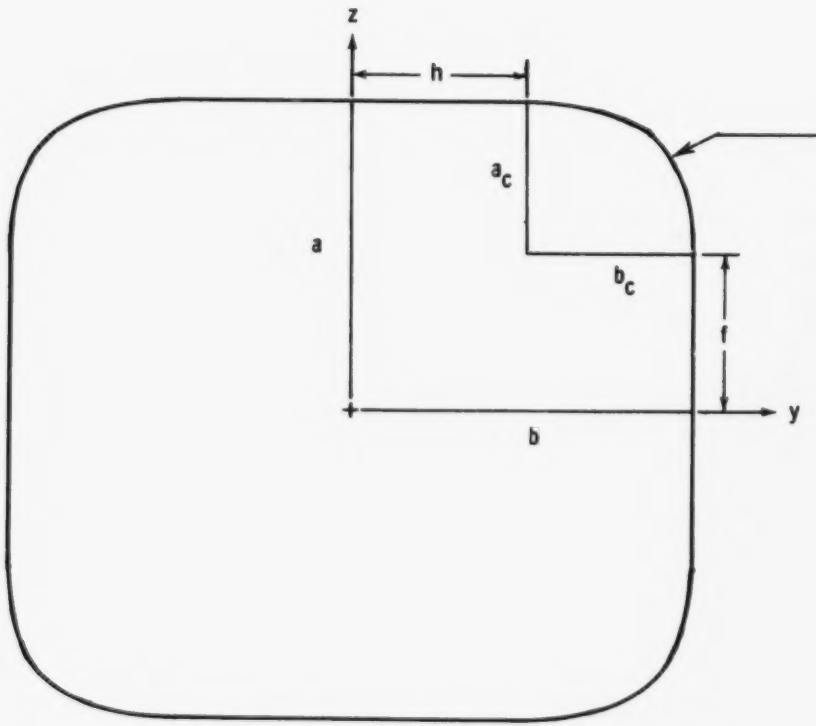

$$\left(\frac{y-h}{b_c}\right)^{\beta} + \left(\frac{z-f}{a_c}\right)^{\beta} = 1.0$$

x_n	a	b	a_c	b_c	f	h	β
0.0000	3.1000	3.4000	3.1000	3.4000	0.0000	0.0000	9.0000
.3100	3.0956	3.3956	3.0173	3.3097	.0782	.0858	8.8858
.6200	3.0823	3.3823	2.7784	3.0489	.3039	.3334	8.5505
.9300	3.0601	3.3601	2.4099	2.6461	.4502	.7140	8.0163
1.2400	3.0290	3.3290	1.9526	2.1460	1.0764	1.1830	7.3215
1.5500	2.9888	3.2915	1.4561	1.6036	1.5327	1.6879	6.4600
1.8600	2.9395	3.2539	.9745	1.0787	1.9650	2.1752	5.3519
2.1700	2.8810	3.2162	.5636	.6292	2.3174	2.5870	4.0783
2.4800	2.8130	3.1785	.2696	.3046	2.5434	2.8739	2.8035
2.7900	2.7355	3.1408	.1227	.1408	2.6128	3.0000	2.0066
3.1000	2.6482	3.1032	.1067	.1250	2.5415	2.9782	2.0000
3.4100	2.5517	3.0655	.1040	.1250	2.4476	2.9405	2.0000
3.7200	2.4536	3.0278	.1013	.1250	2.3523	2.9028	2.0000
4.0300	2.3555	2.9901	.0985	.1250	2.2570	2.8651	2.0000
4.3400	2.2574	2.9525	.0956	.1250	2.1618	2.8275	2.0000
4.6500	2.1592	2.9148	.0926	.1250	2.0666	2.7898	2.0000
4.9600	2.0611	2.8771	.0895	.1250	1.9716	2.7521	2.0000
5.2700	1.9630	2.8394	.0864	.1250	1.8766	2.7144	2.0000
5.5800	1.8649	2.8017	.0832	.1250	1.7817	2.6767	2.0000
5.8900	1.7668	2.7641	.0799	.1250	1.6869	2.6391	2.0000
6.2000	1.6687	2.7264	.0765	.1250	1.5922	2.6014	2.0000
6.5100	1.5706	2.6887	.0730	.1250	1.4976	2.5637	2.0000
6.8200	1.4725	2.6510	.0694	.1250	1.4030	2.5260	2.0000
7.2400	1.3395	2.6000	.0644	.1250	1.2751	2.4750	2.0000

(c) Nozzle external cross-sectional geometry.

Figure 4. Concluded.

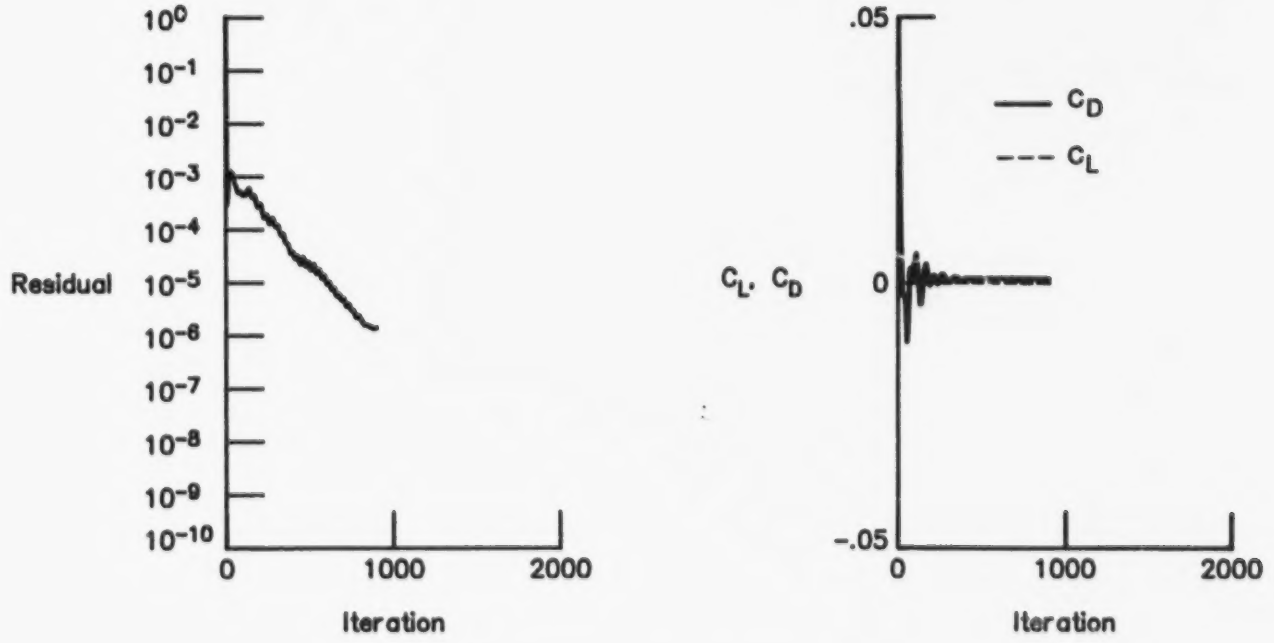

(a) Convergence properties.

Figure 5. Convergence properties and solution at a Mach number of 0.60. Turbulent solution; $R_\ell = 17.2 \times 10^6$; fine grid.

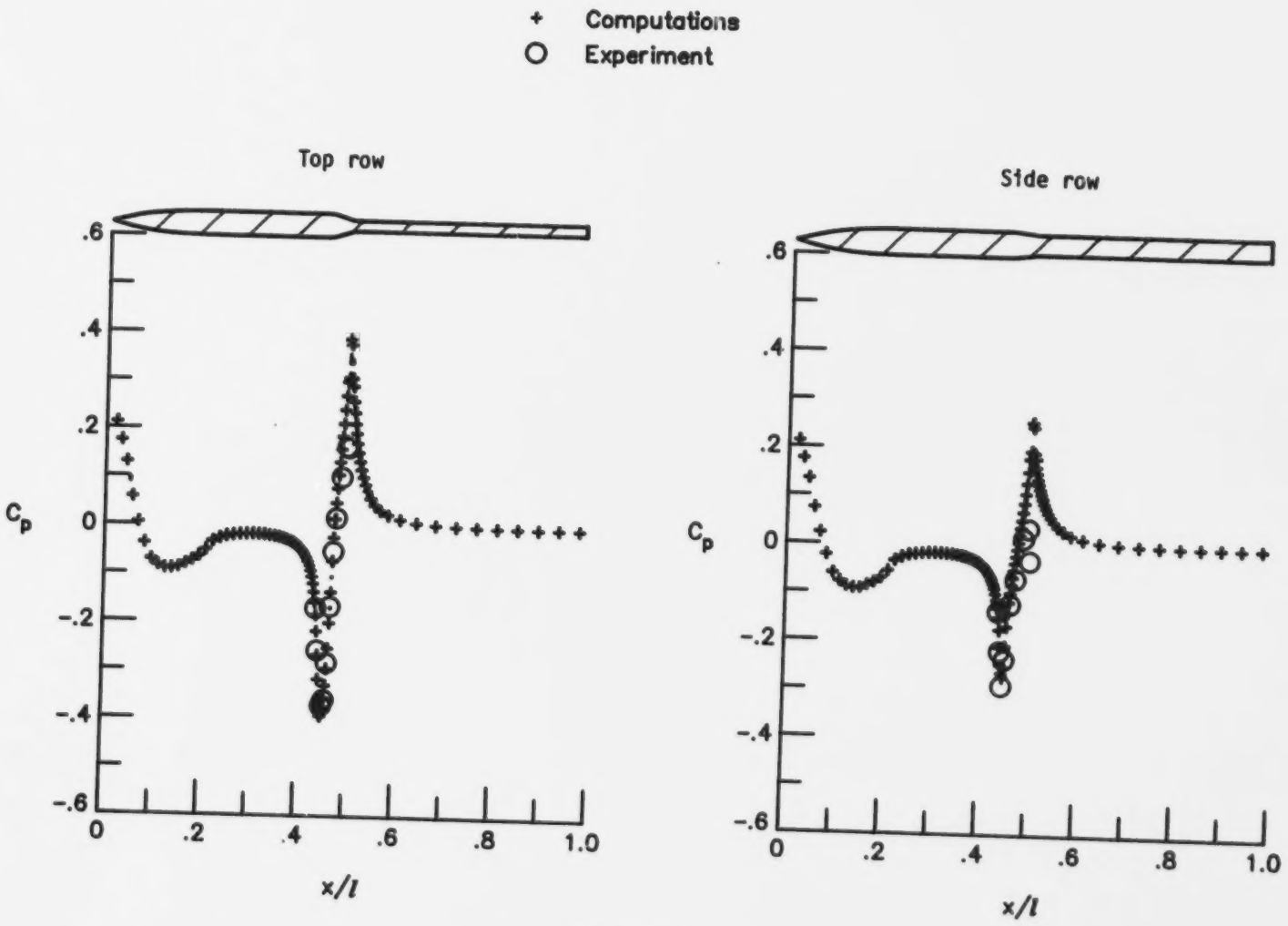

(b) Solution.

Figure 5. Concluded.

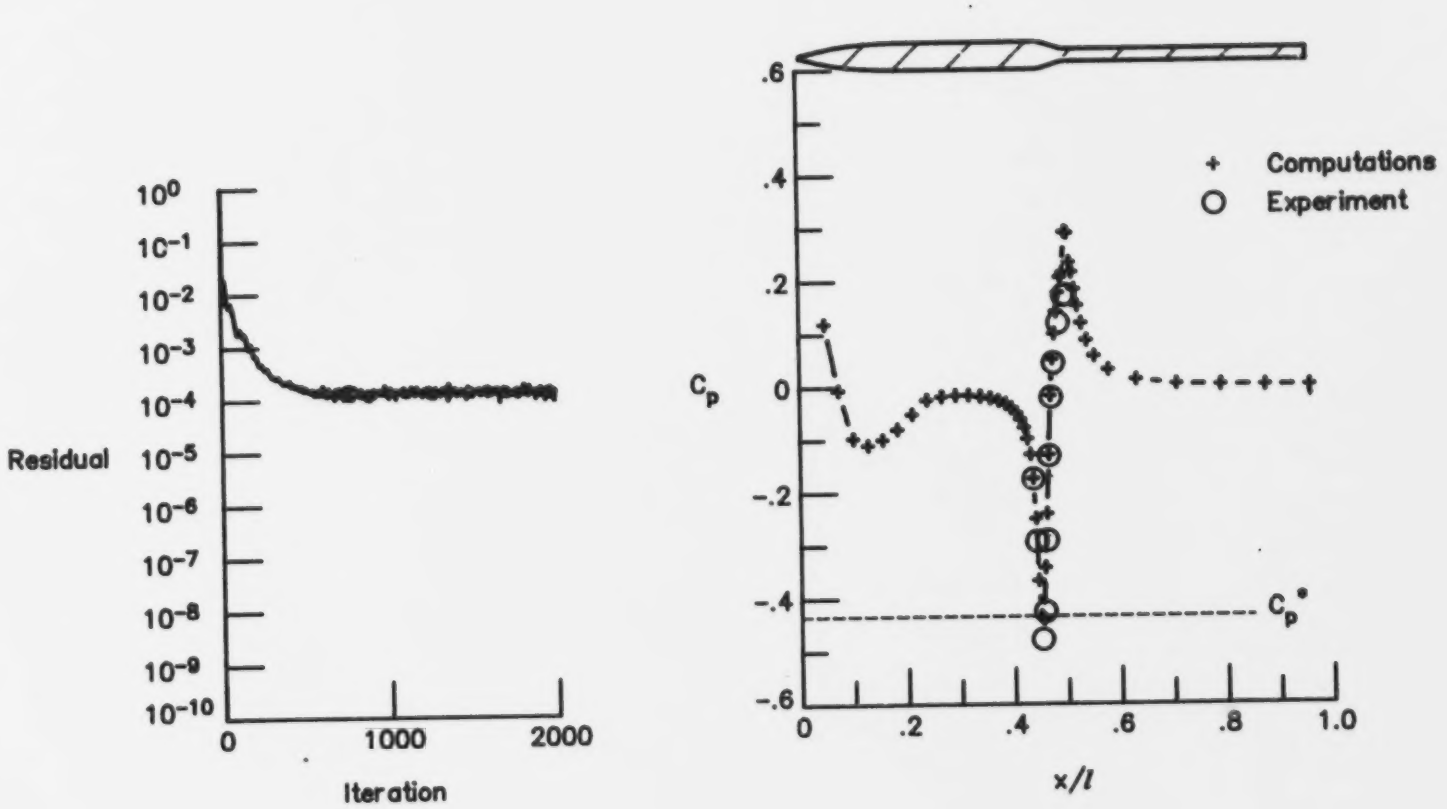

Figure 6. Convergence properties and solution at Mach number of 0.80. Turbulent solution; $R_\ell = 19.5 \times 10^6$; coarse grid.

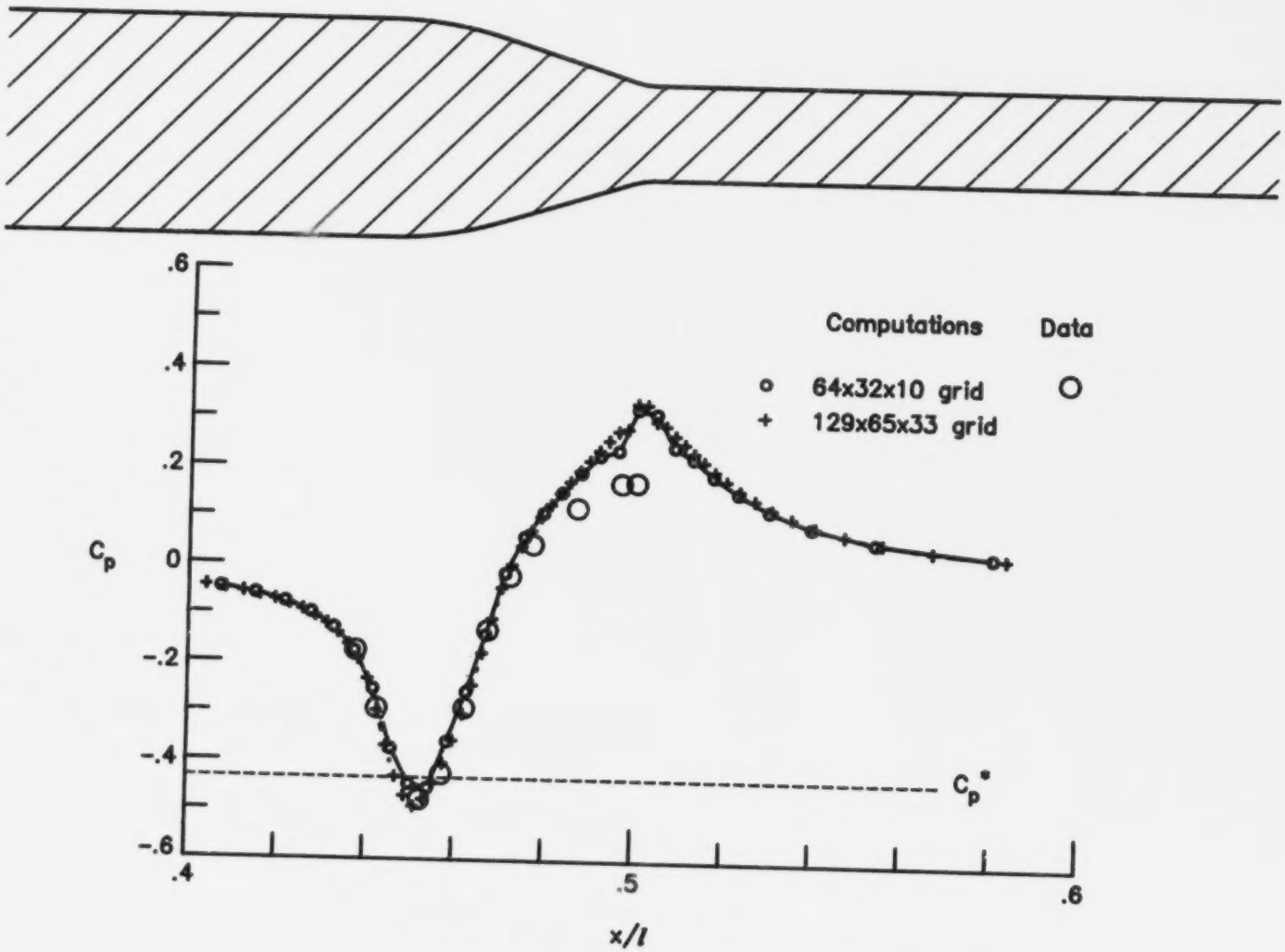

(a) Top row.

Figure 7. Comparison of coarse ($64 \times 32 \times 10$) grid and fine ($129 \times 65 \times 33$) grid solutions. $M_\infty = 0.80$; turbulent flow; $R_\ell = 19.5 \times 10^6$.

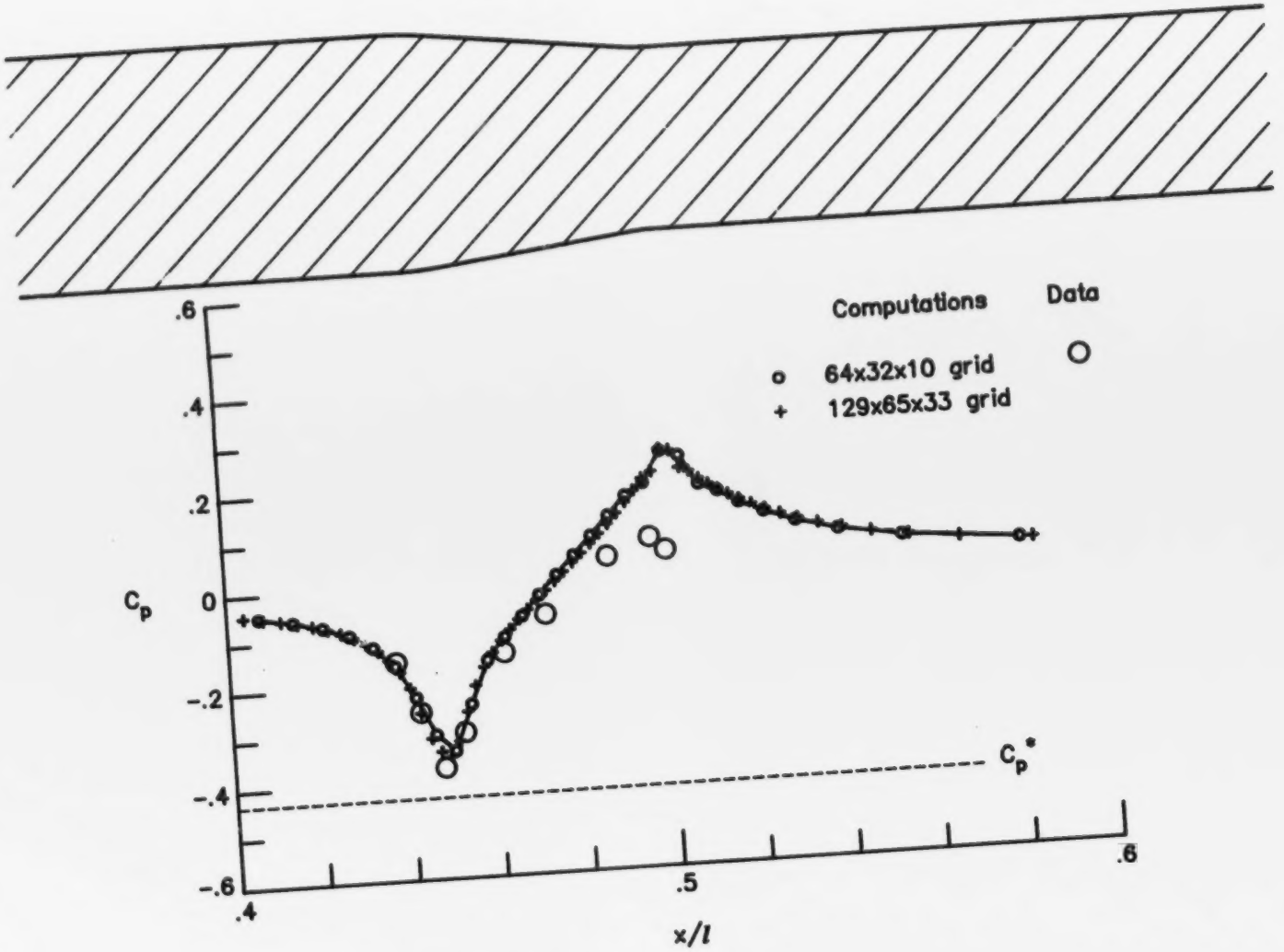

(b) Side row.

Figure 7. Continued.

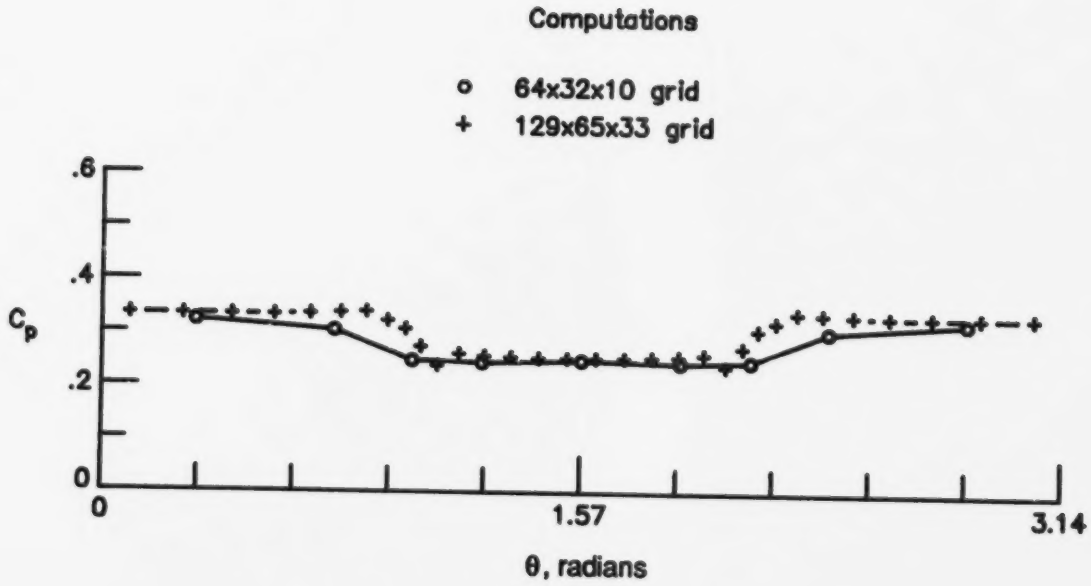

(c) Cross-plane distributions; $x/l = 0.50$ (nozzle exit).

Figure 7. Concluded.

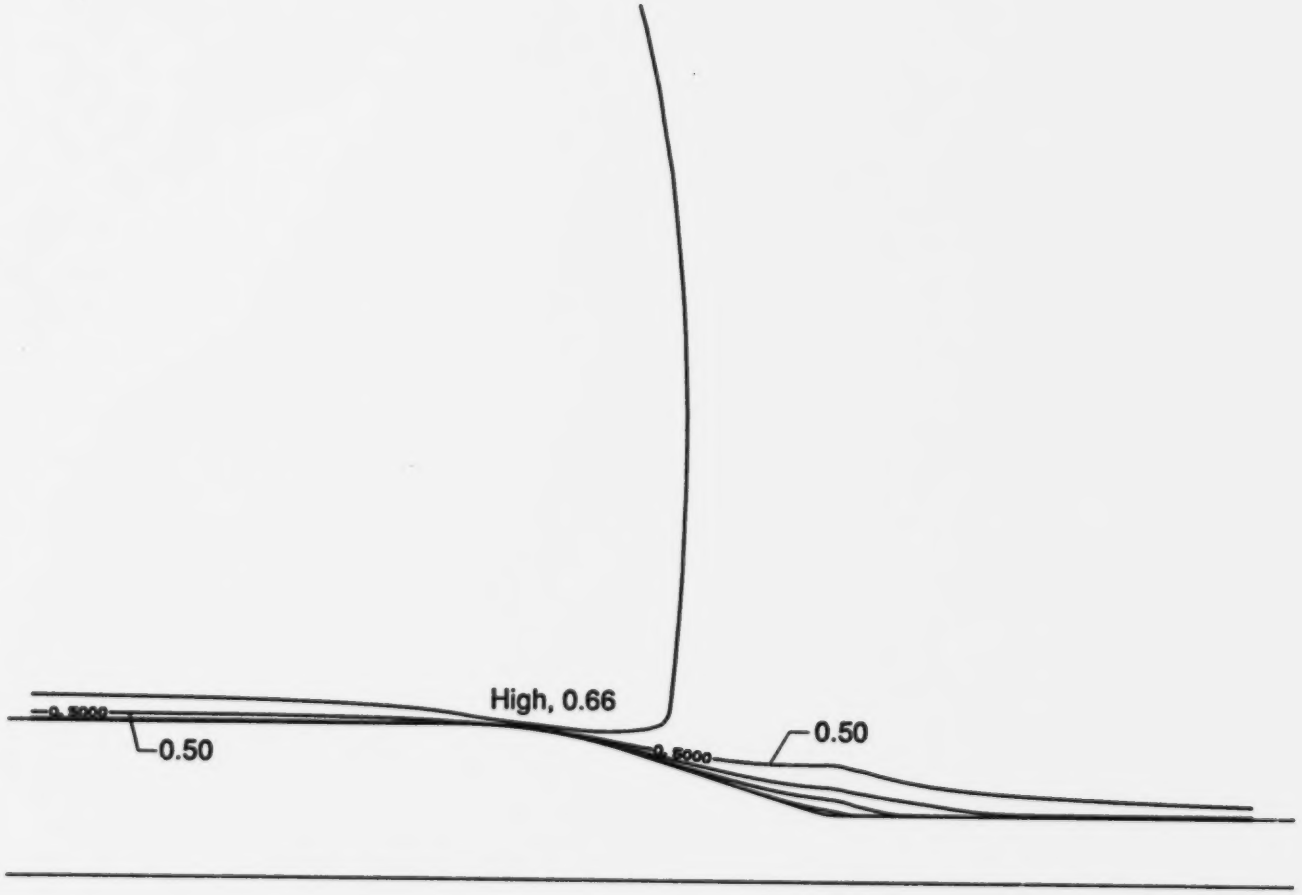

(a) Mach number contours, top row; contour increment, 0.10.

Figure 8. Details of afterbody solution at free-stream Mach number of 0.60. Turbulent flow; $R_\ell = 17.2 \times 10^6$; fine grid.

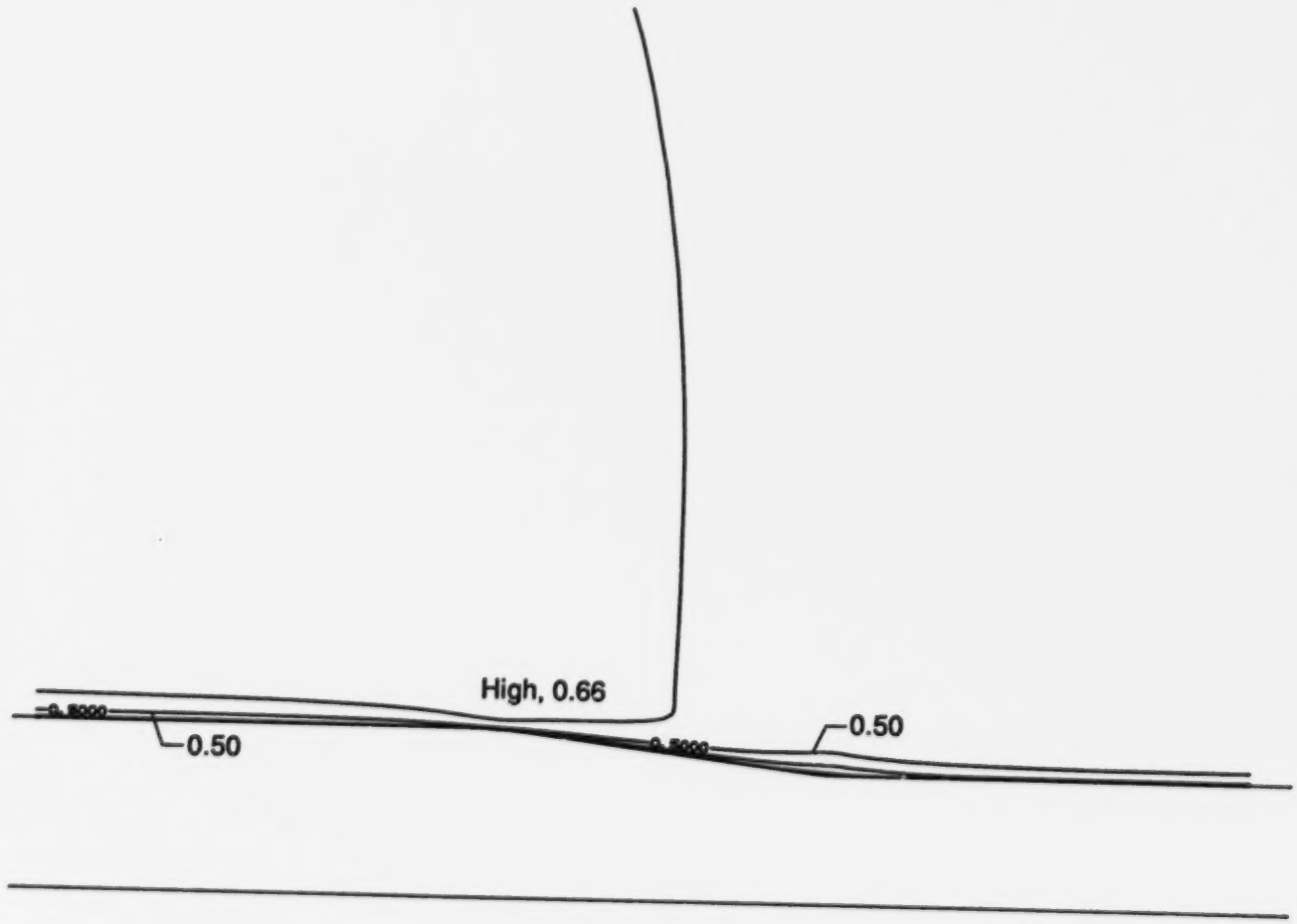

(b) Mach number contours, side row; contour increment, 0.10.

Figure 8. Continued.

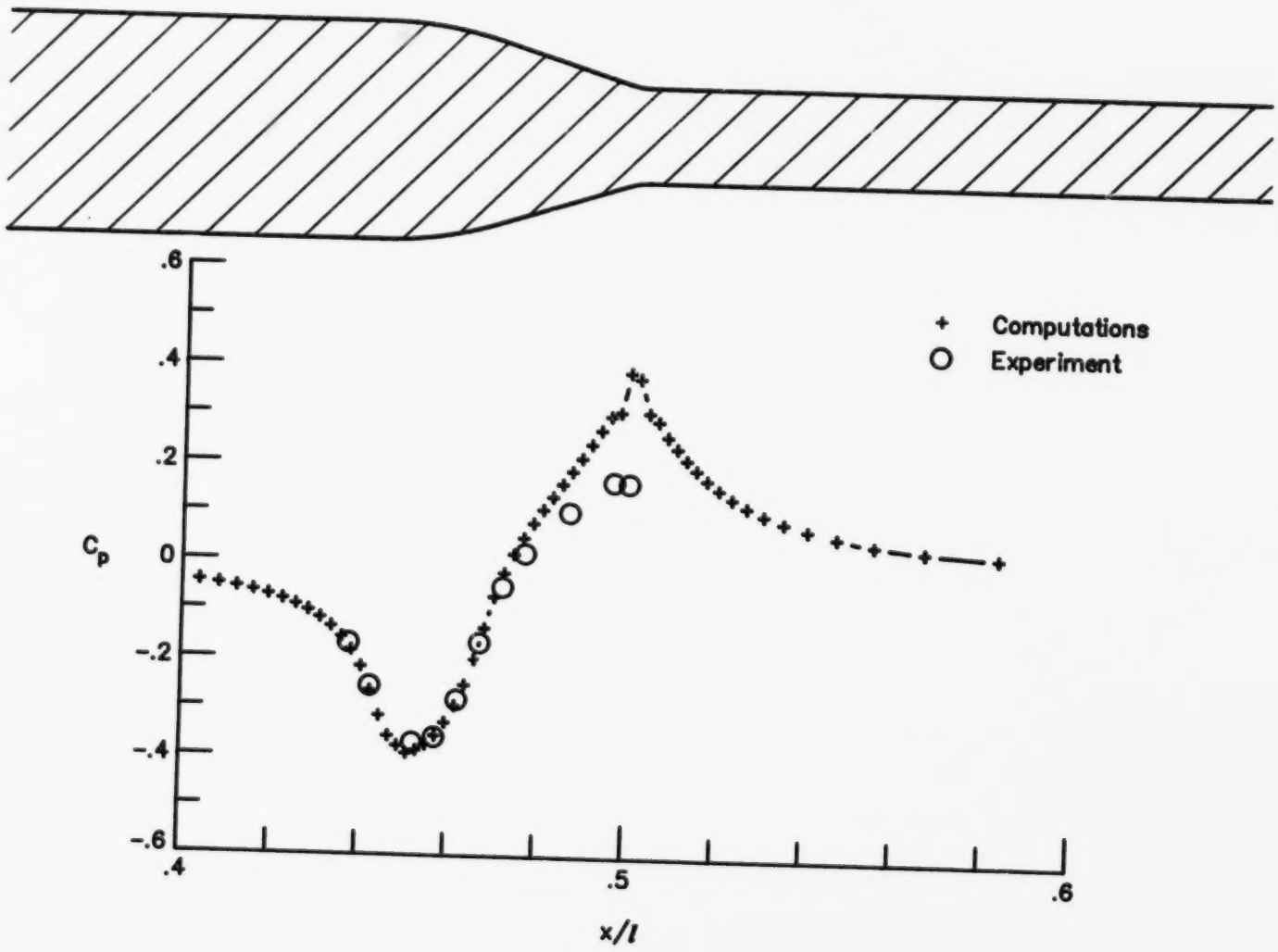

(c) Pressure distributions, top row.

Figure 8. Continued.

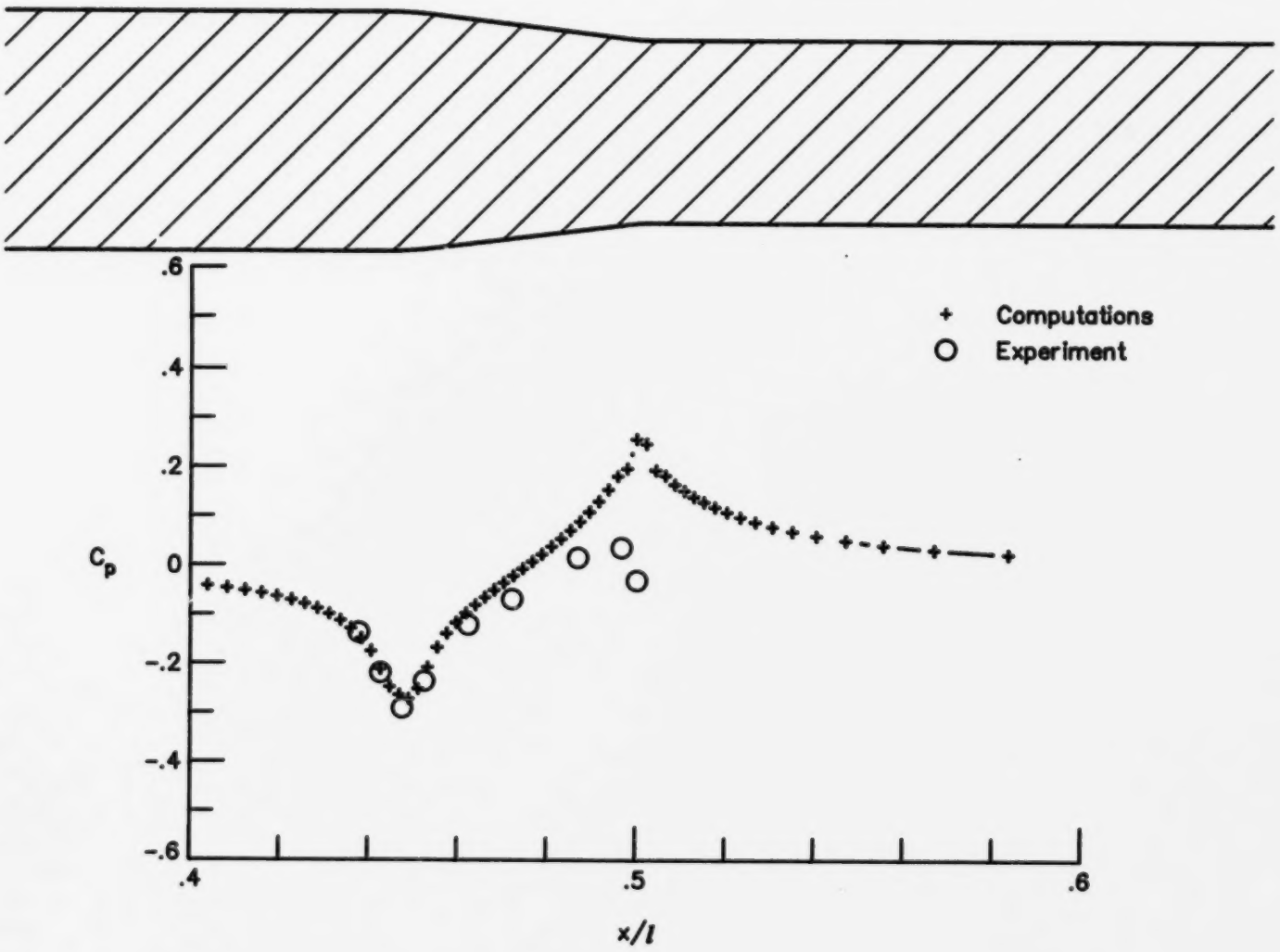

(d) Pressure distributions, side row.

Figure 8. Continued.

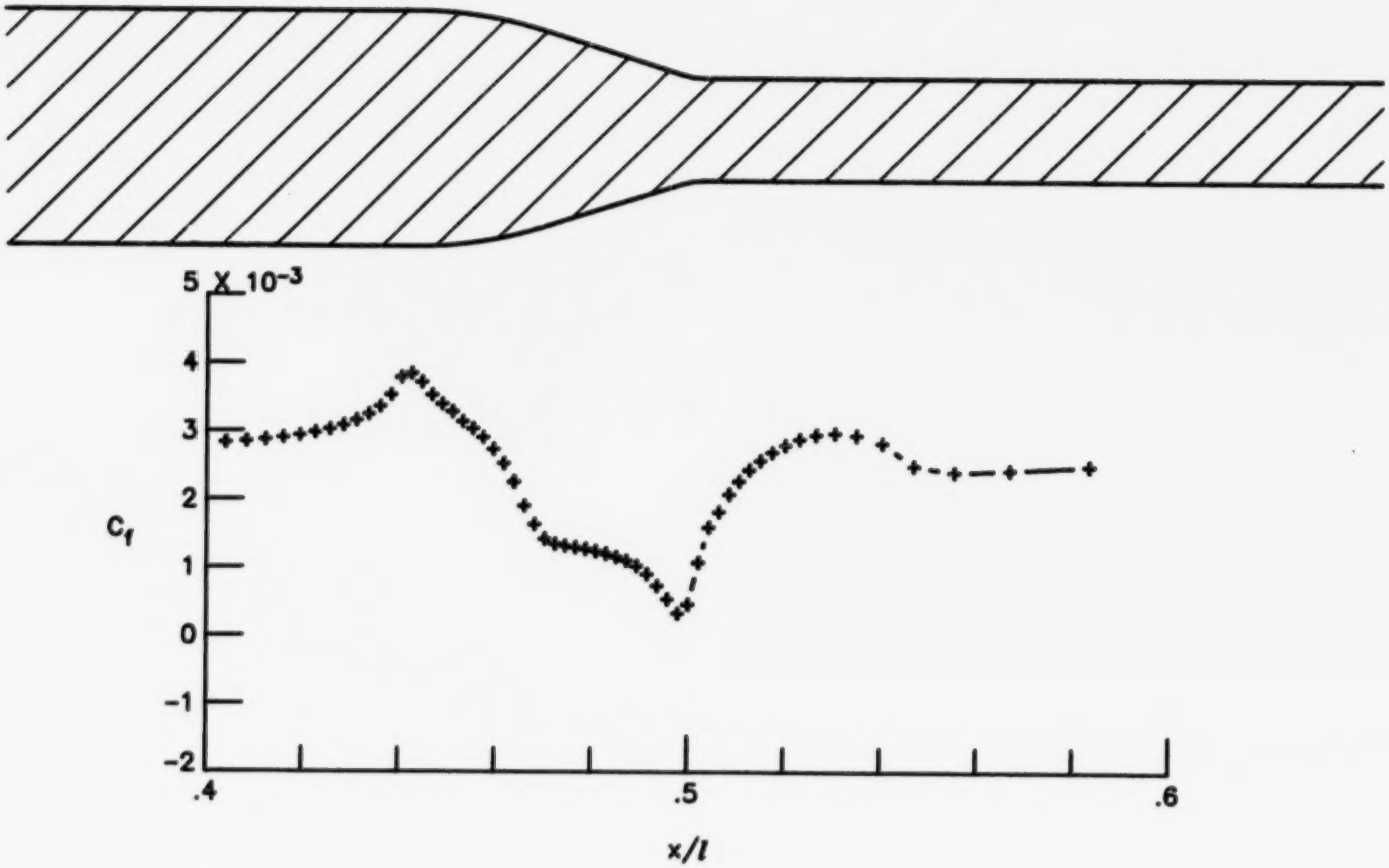

(e) Skin friction distributions, top row.

Figure 8. Continued.

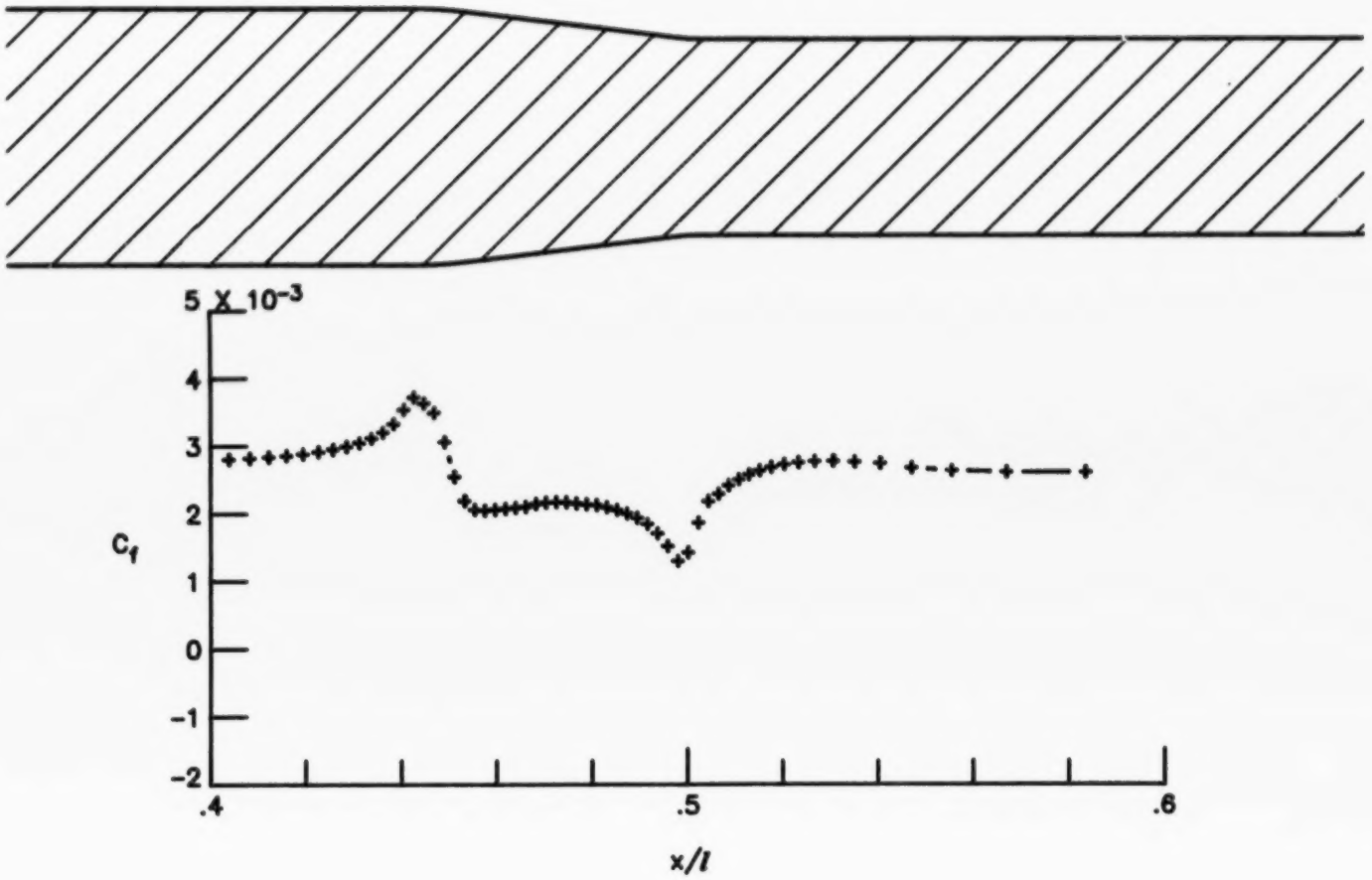

(f) Skin friction distributions, side row.

Figure 8. Concluded.

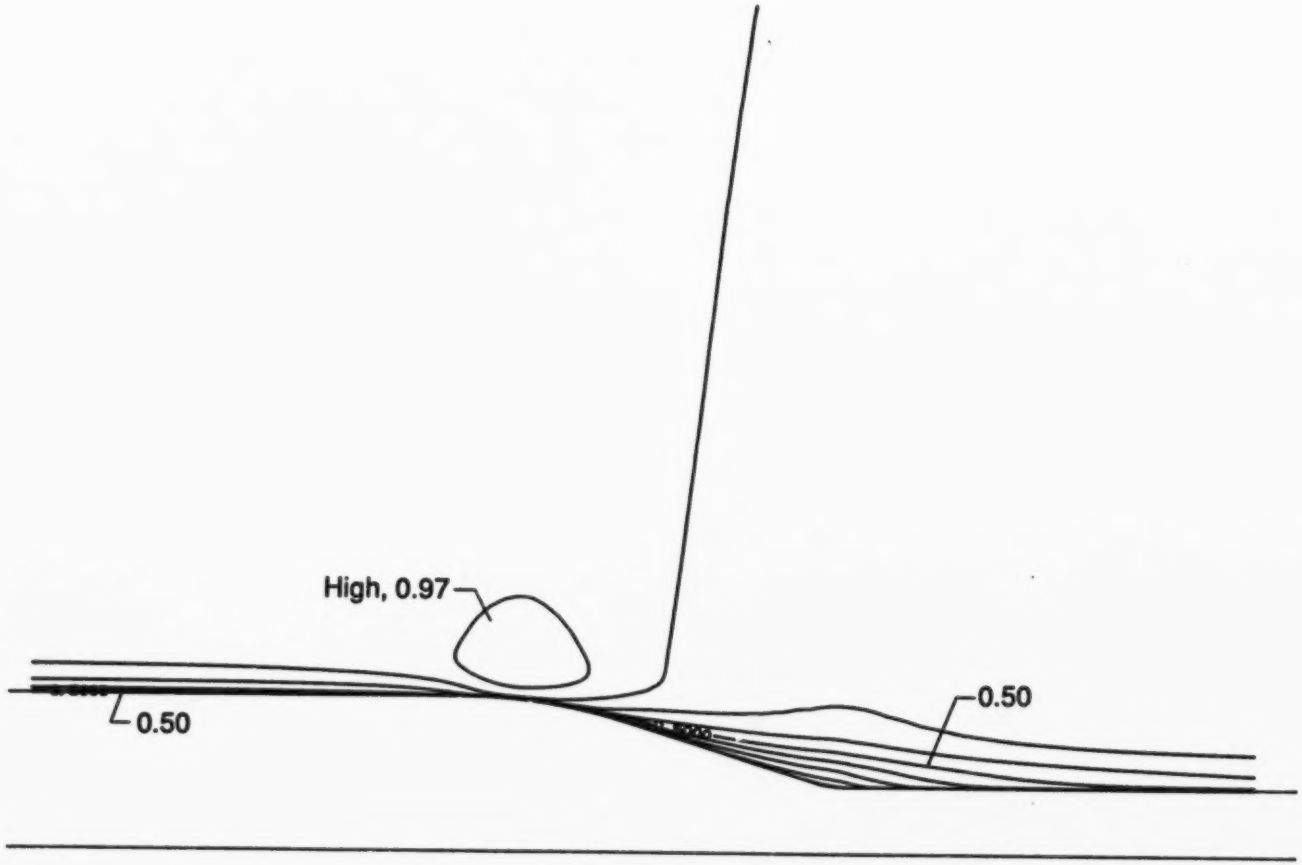

(a) Mach number contours, top row; contour increment, 0.10.

Figure 9. Details of afterbody solution at free-stream Mach number of 0.80. Turbulent flow; $R_\ell = 19.5 \times 10^6$; fine grid.

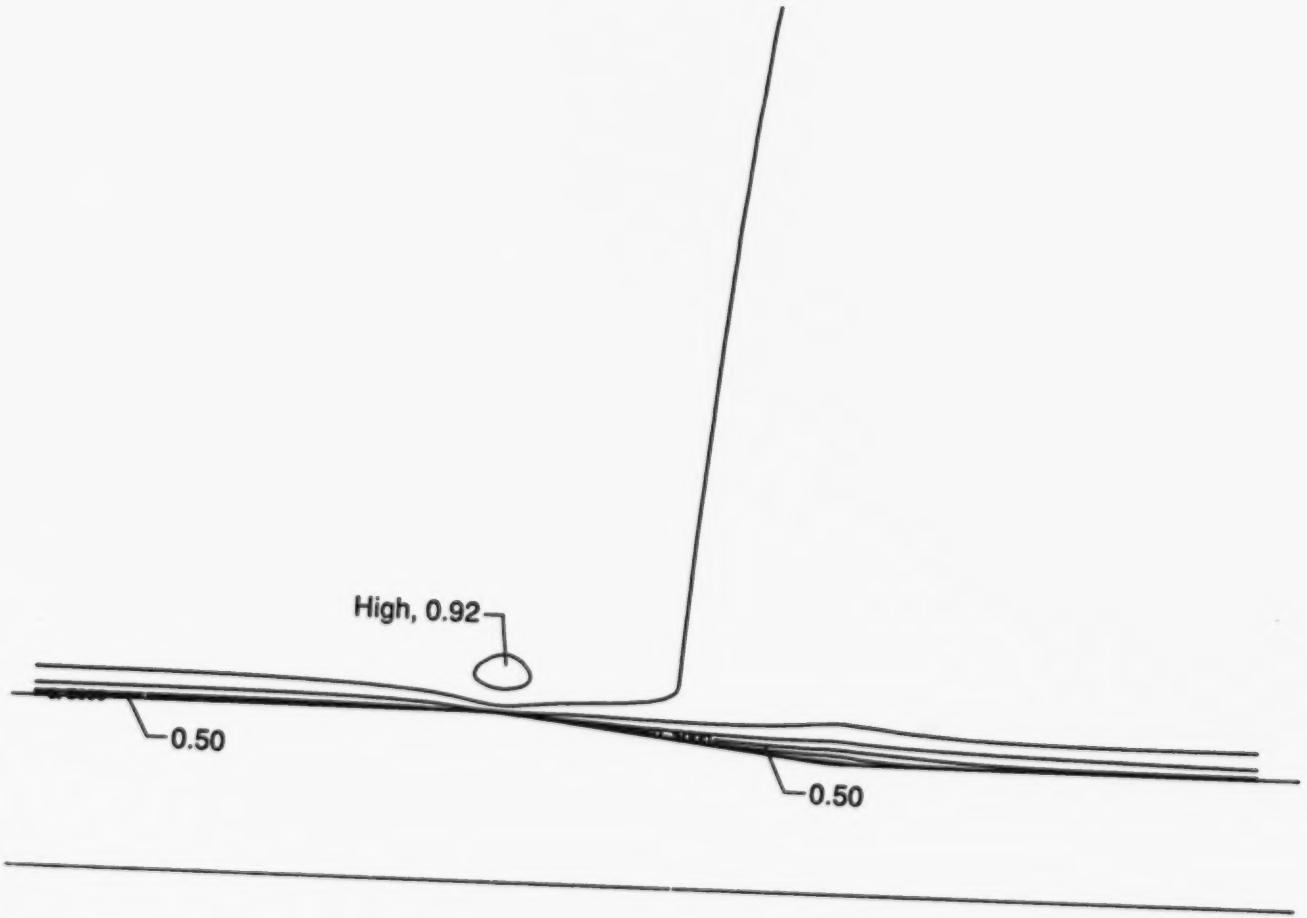

(b) Mach number contours, side row; contour increment, 0.10.

Figure 9. Continued.

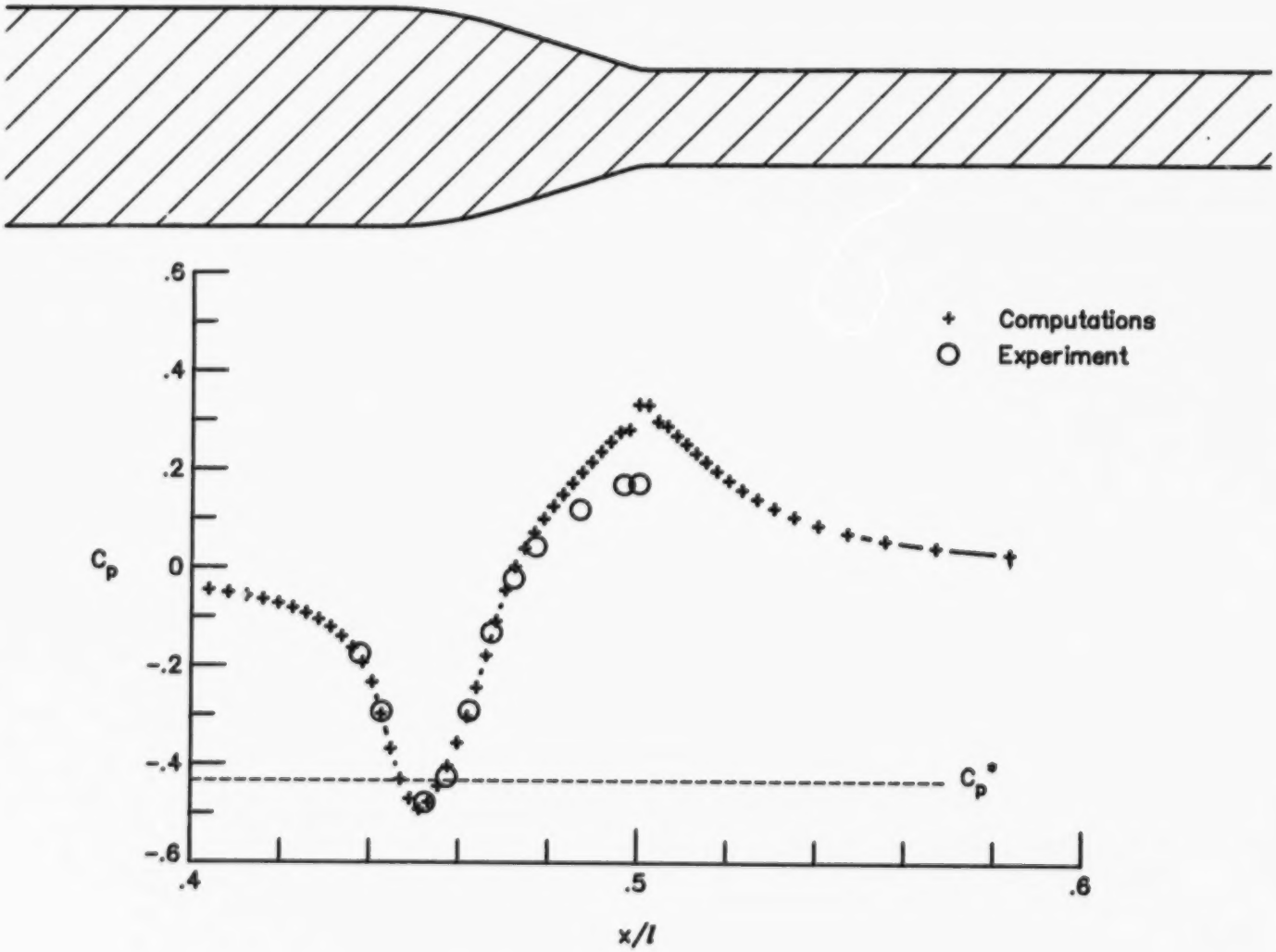

(c) Pressure distributions, top row.

Figure 9. Continued.

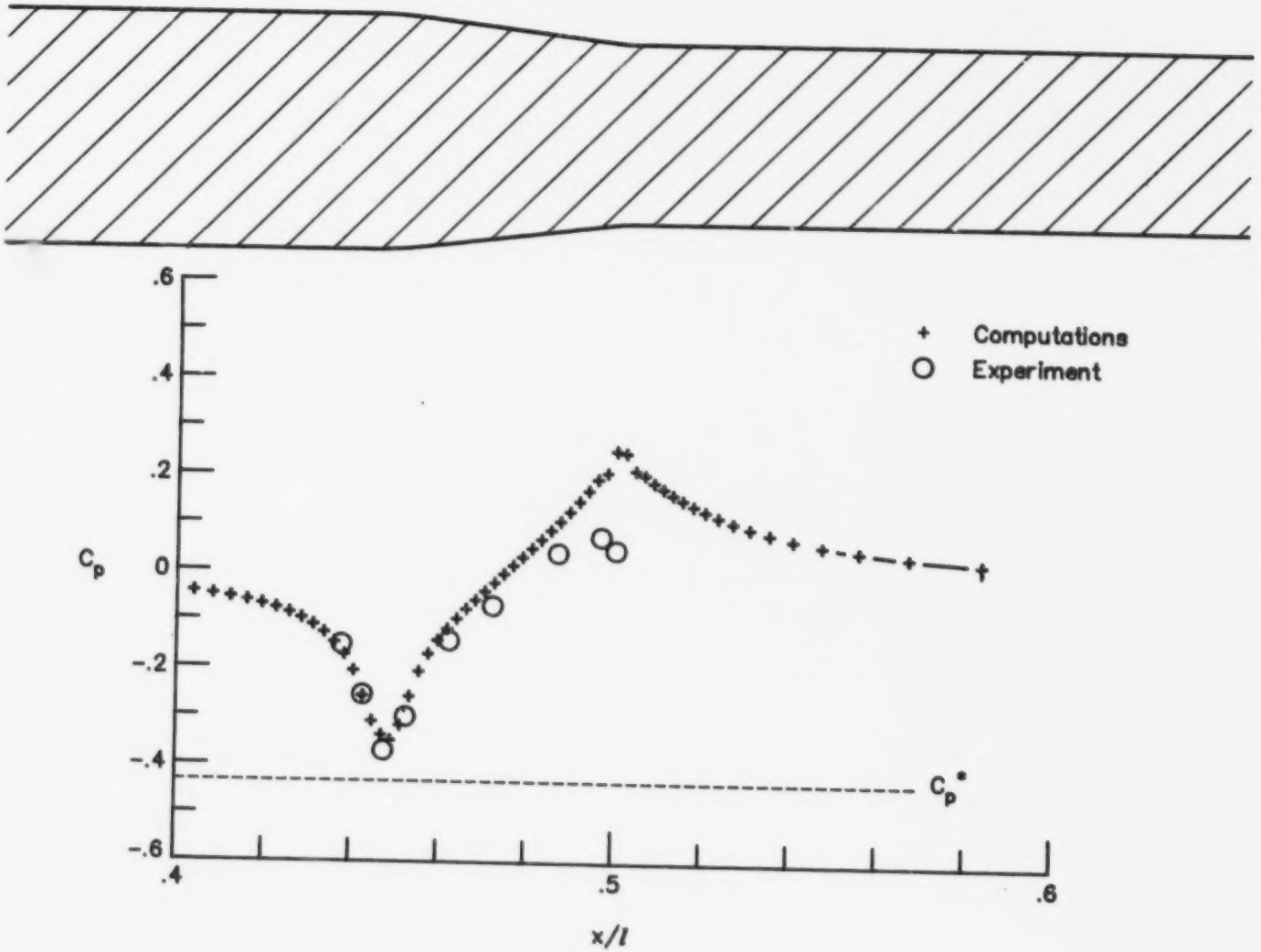

(d) Pressure distributions, side row.

Figure 9. Continued.

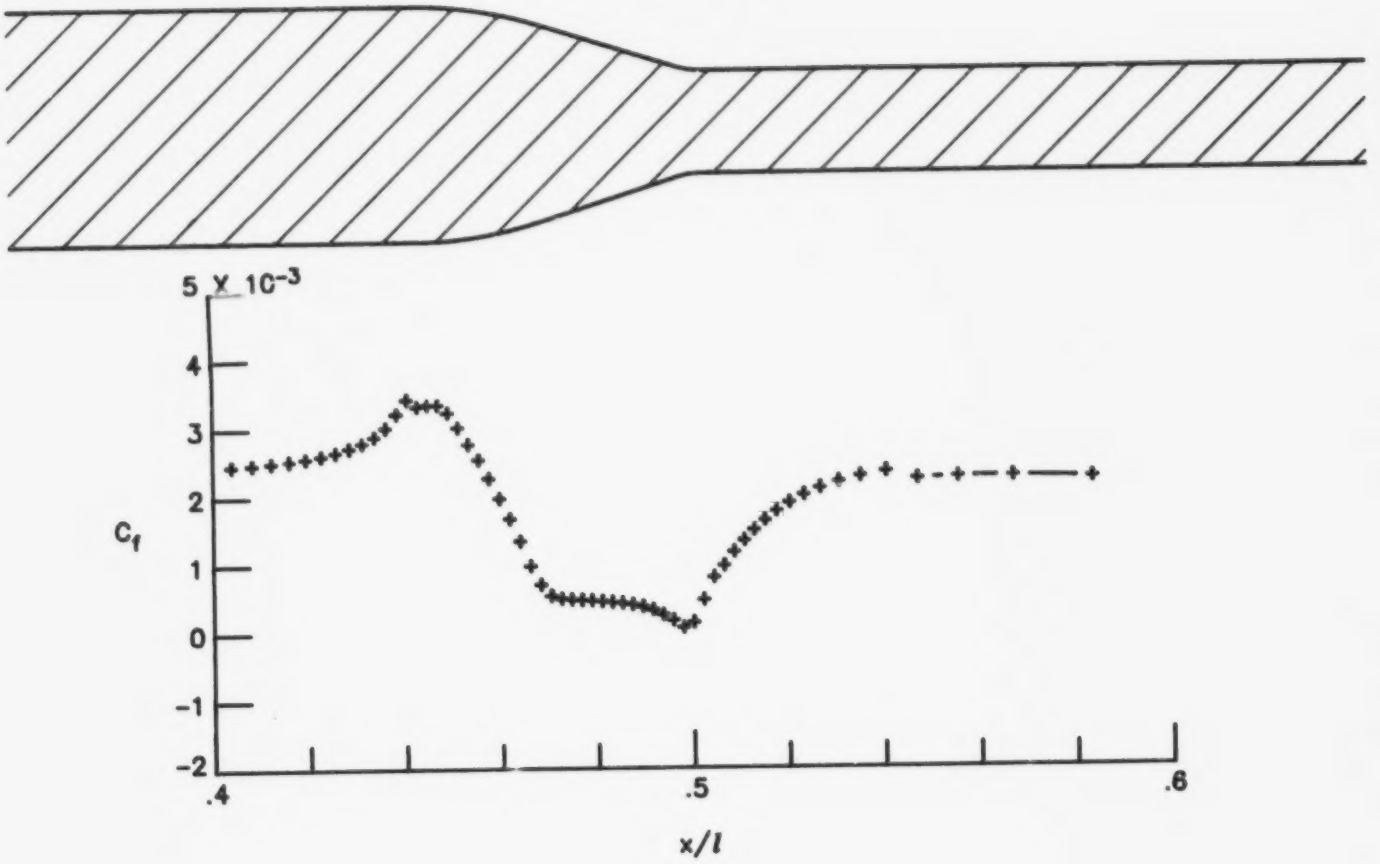

(e) Skin friction distributions, top row.

Figure 9. Continued.

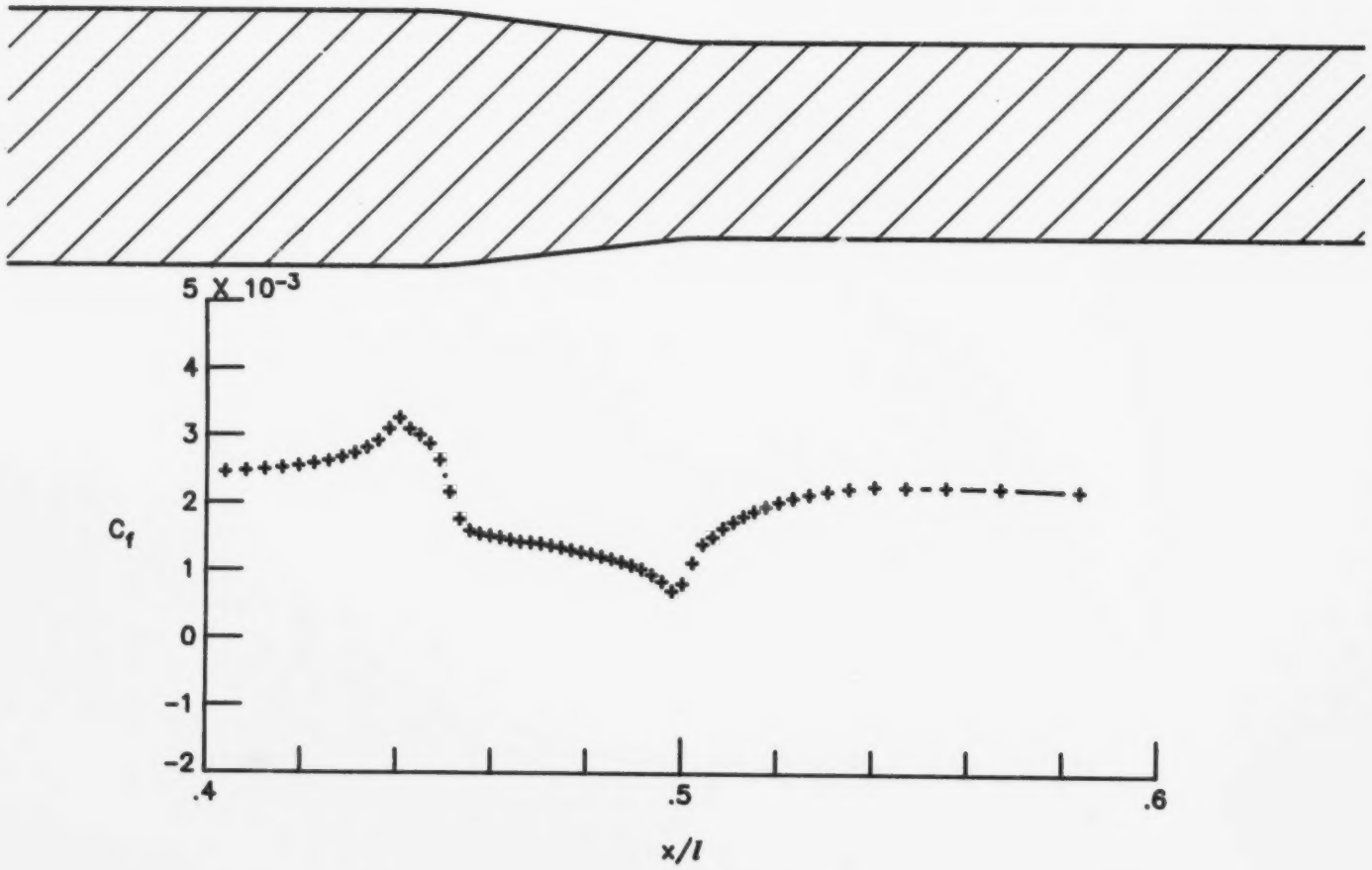

(f) Skin friction distributions, side row.

Figure 9. Concluded.

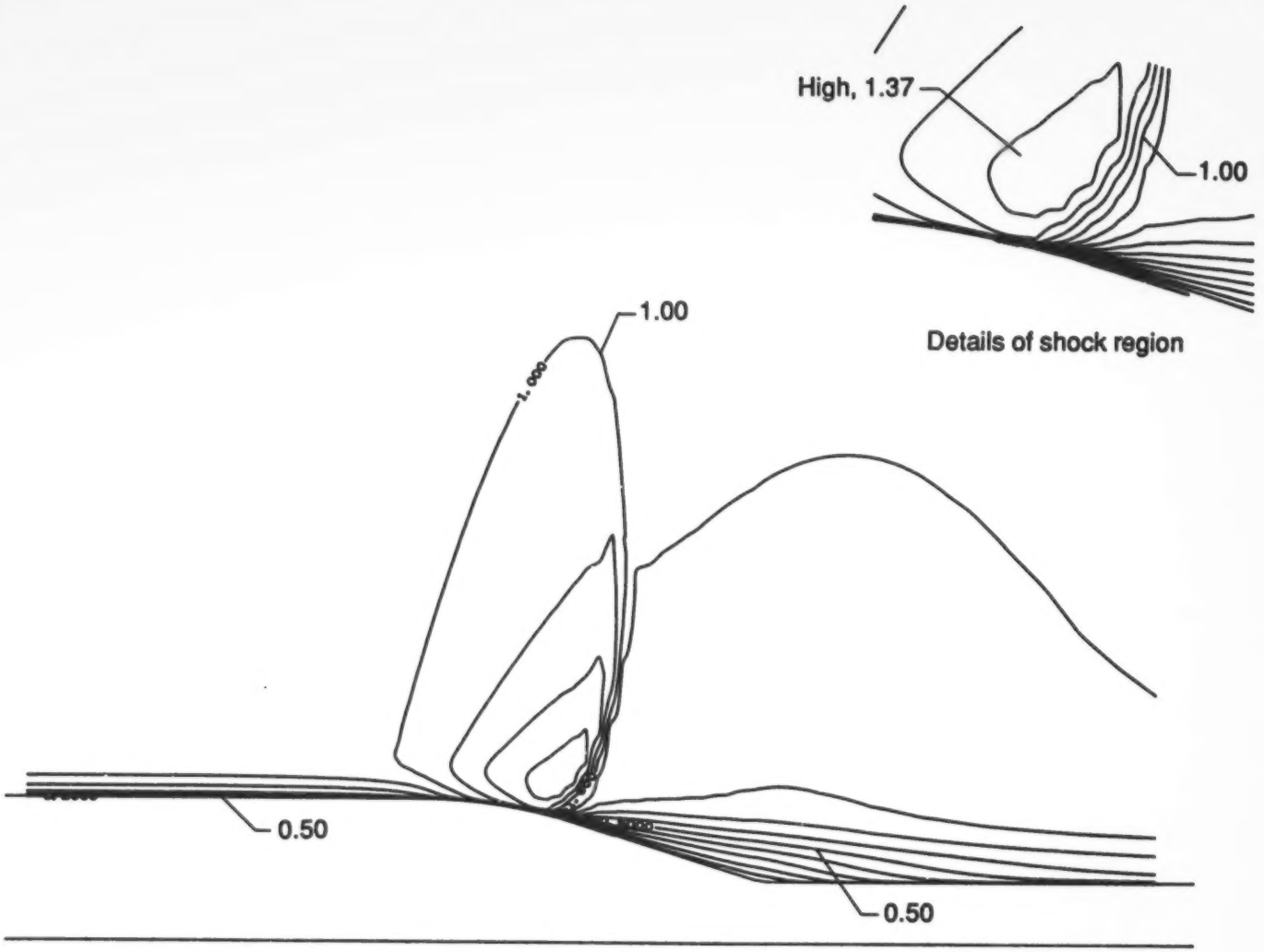

(a) Mach number contours, top row; contour increment, 0.10.

Figure 10. Details of afterbody solution at free-stream Mach number of 0.94. Turbulent flow; $R_\ell = 29.3 \times 10^6$; fine grid.

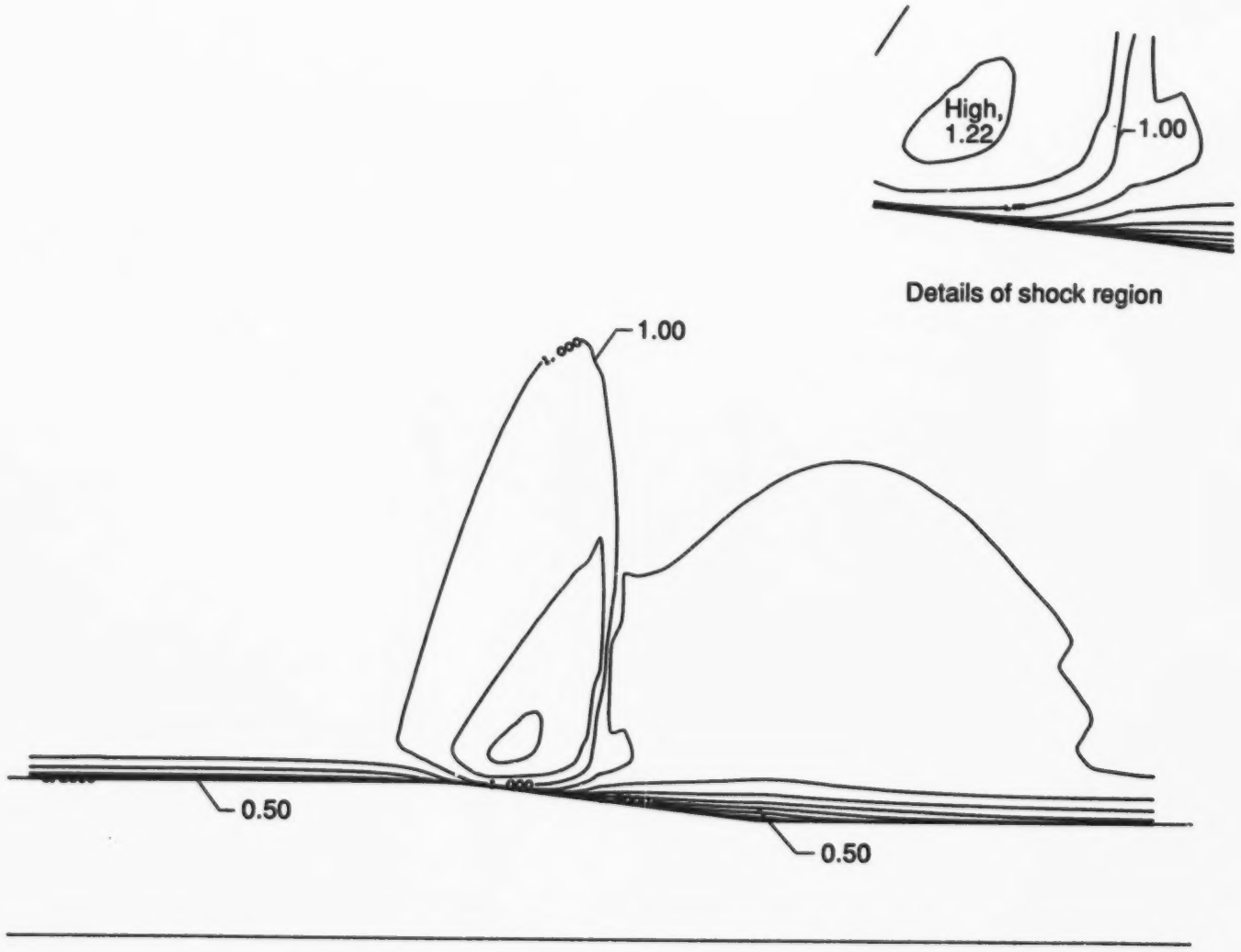

(b) Mach number contours, side row; contour increment, 0.10.

Figure 10. Continued.

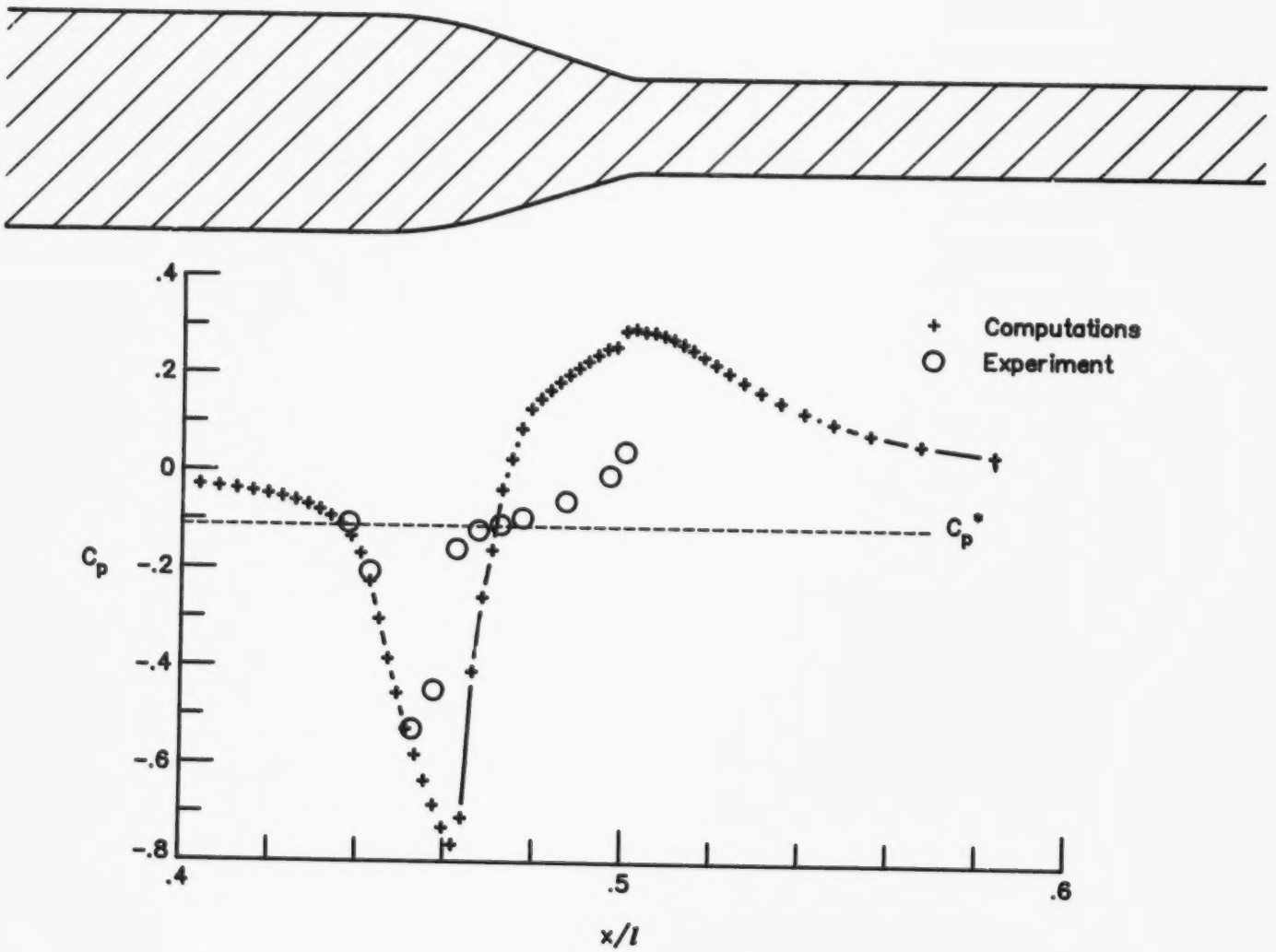

(c) Pressure distributions, top row.

Figure 10. Continued.

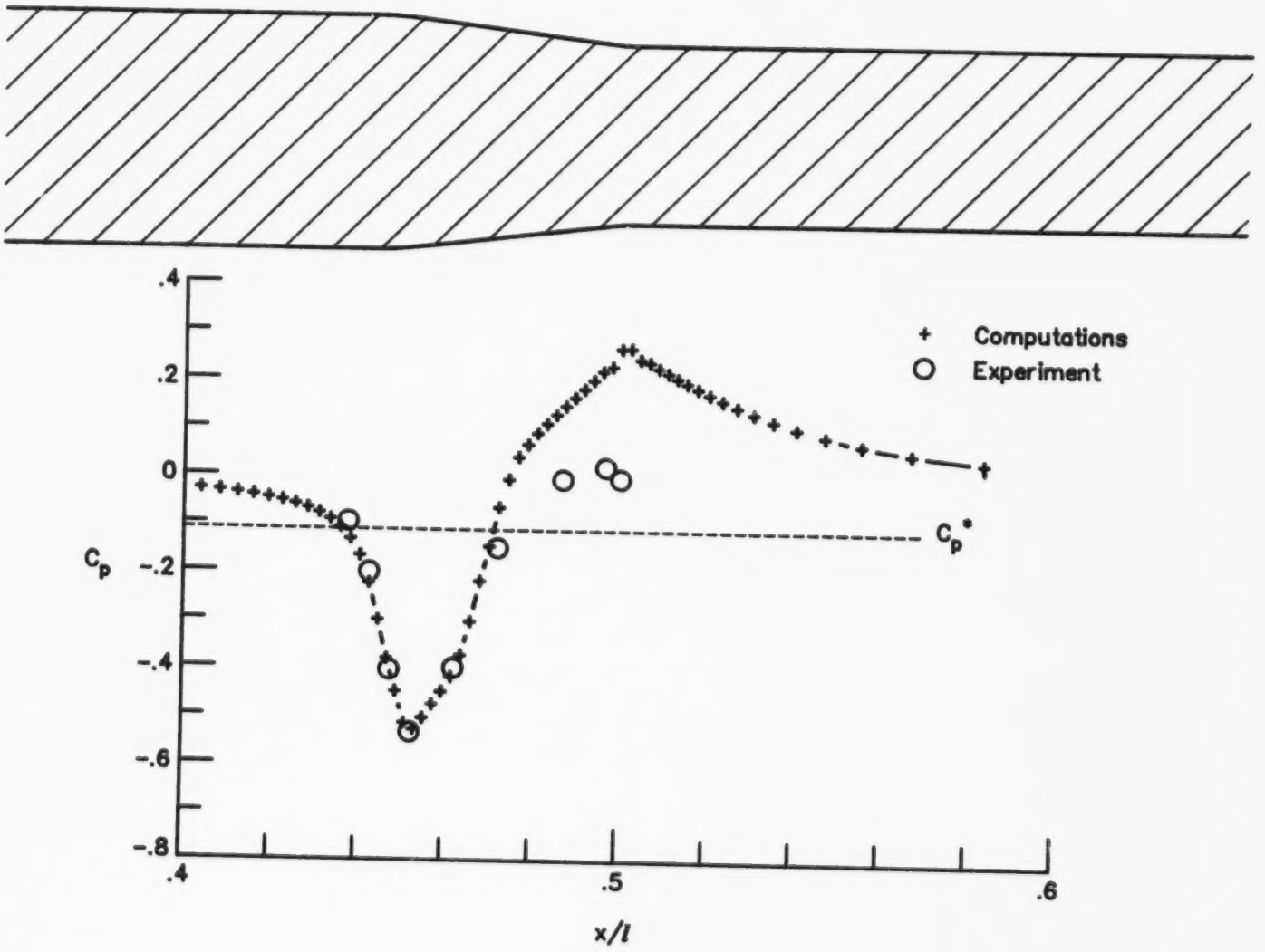

(d) Pressure distributions, side row.

Figure 10. Continued.

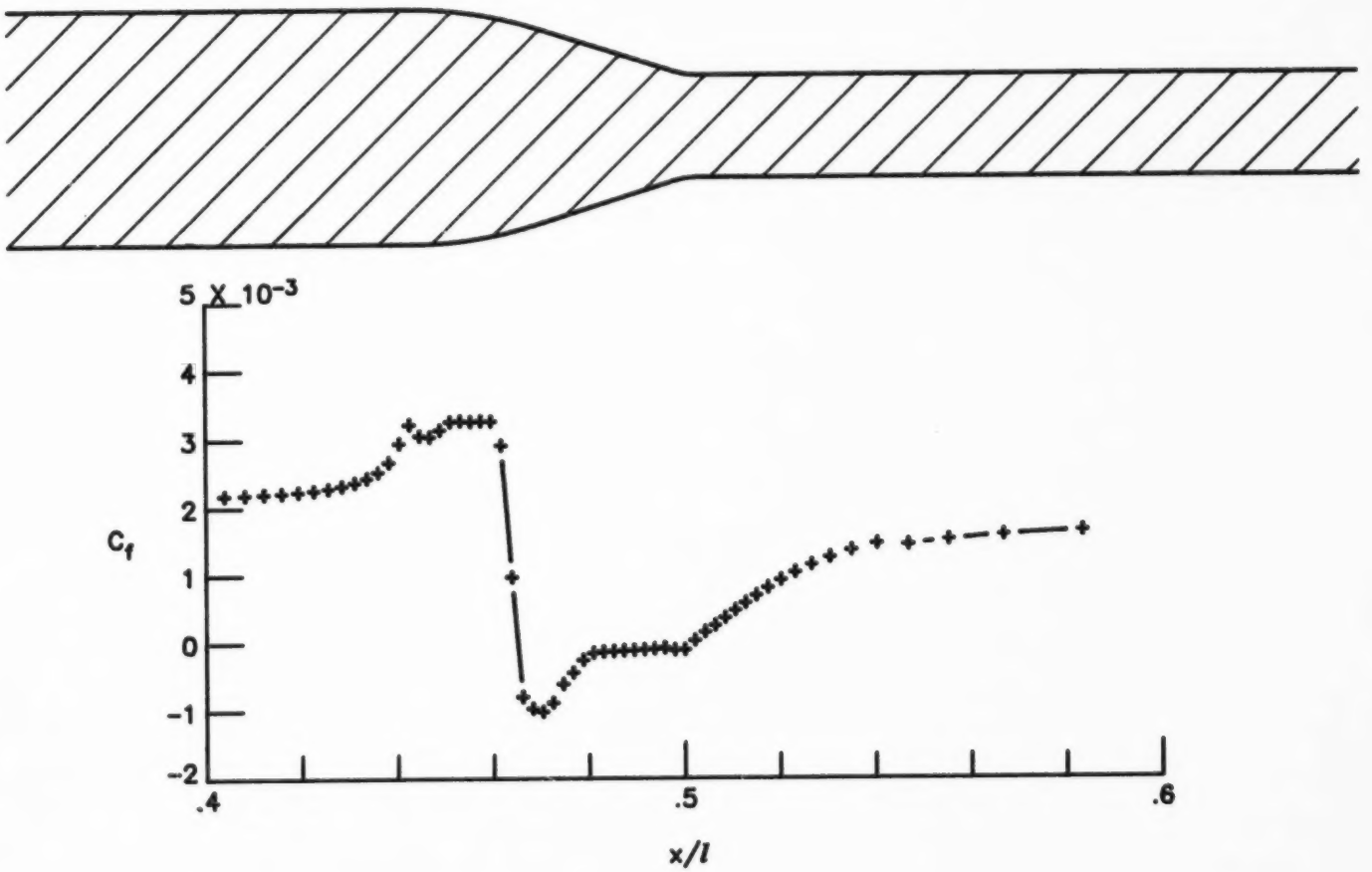

(e) Skin friction distributions, top row.

Figure 10. Continued.

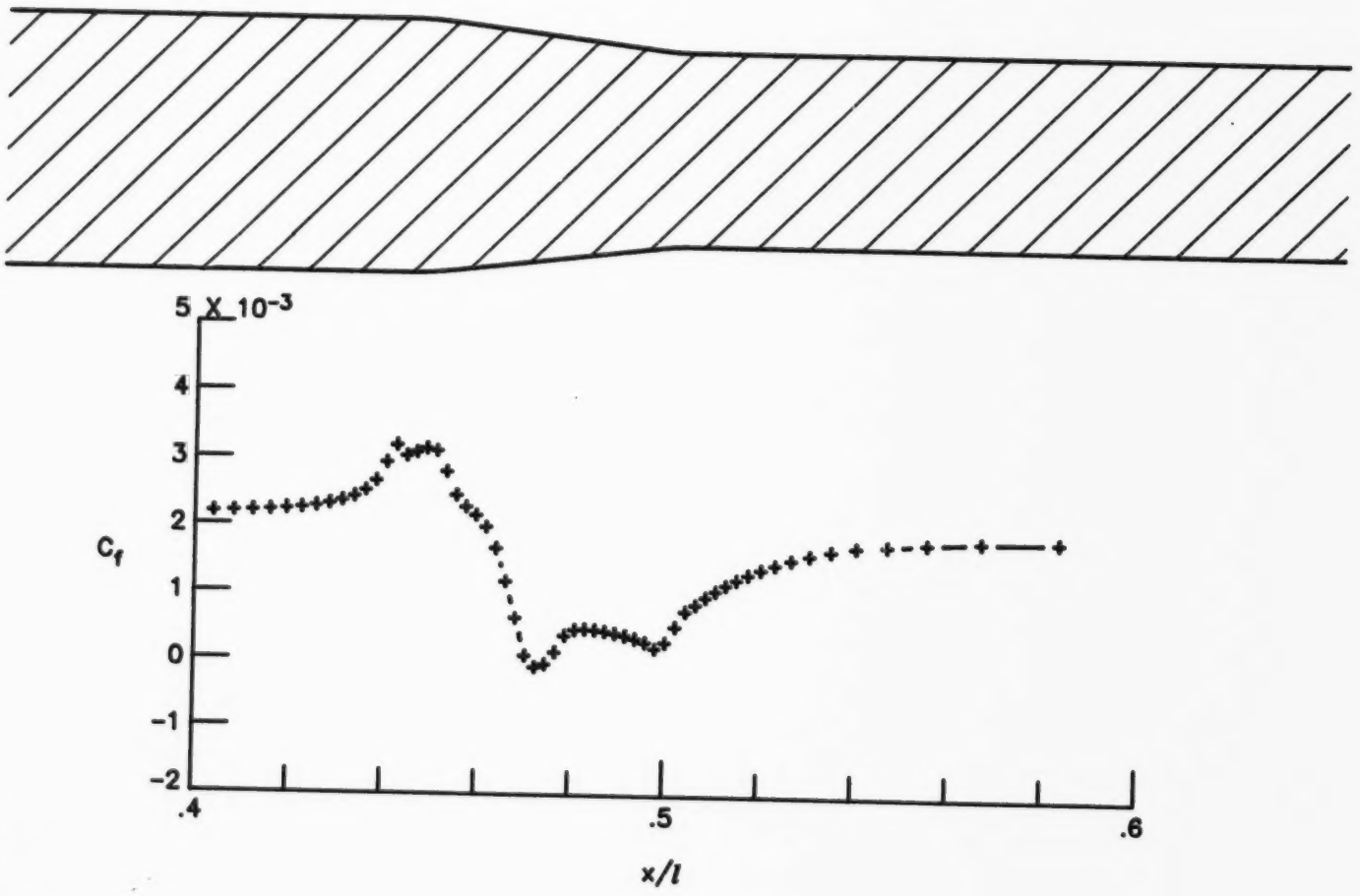

(f) Skin friction distributions, side row.

Figure 10. Concluded.

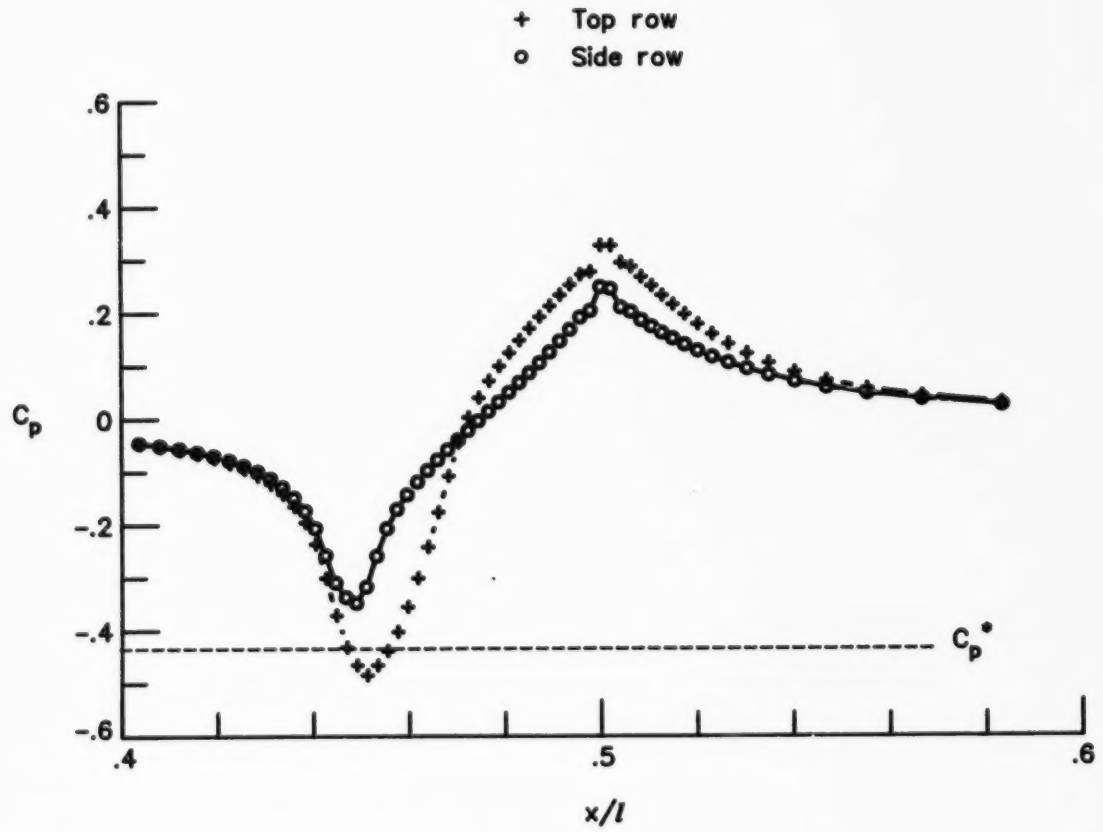

Figure 11. Computed afterbody pressures along top and side rows. $M_\infty = 0.80$; turbulent flow; $R_\ell = 19.5 \times 10^6$; fine grid.

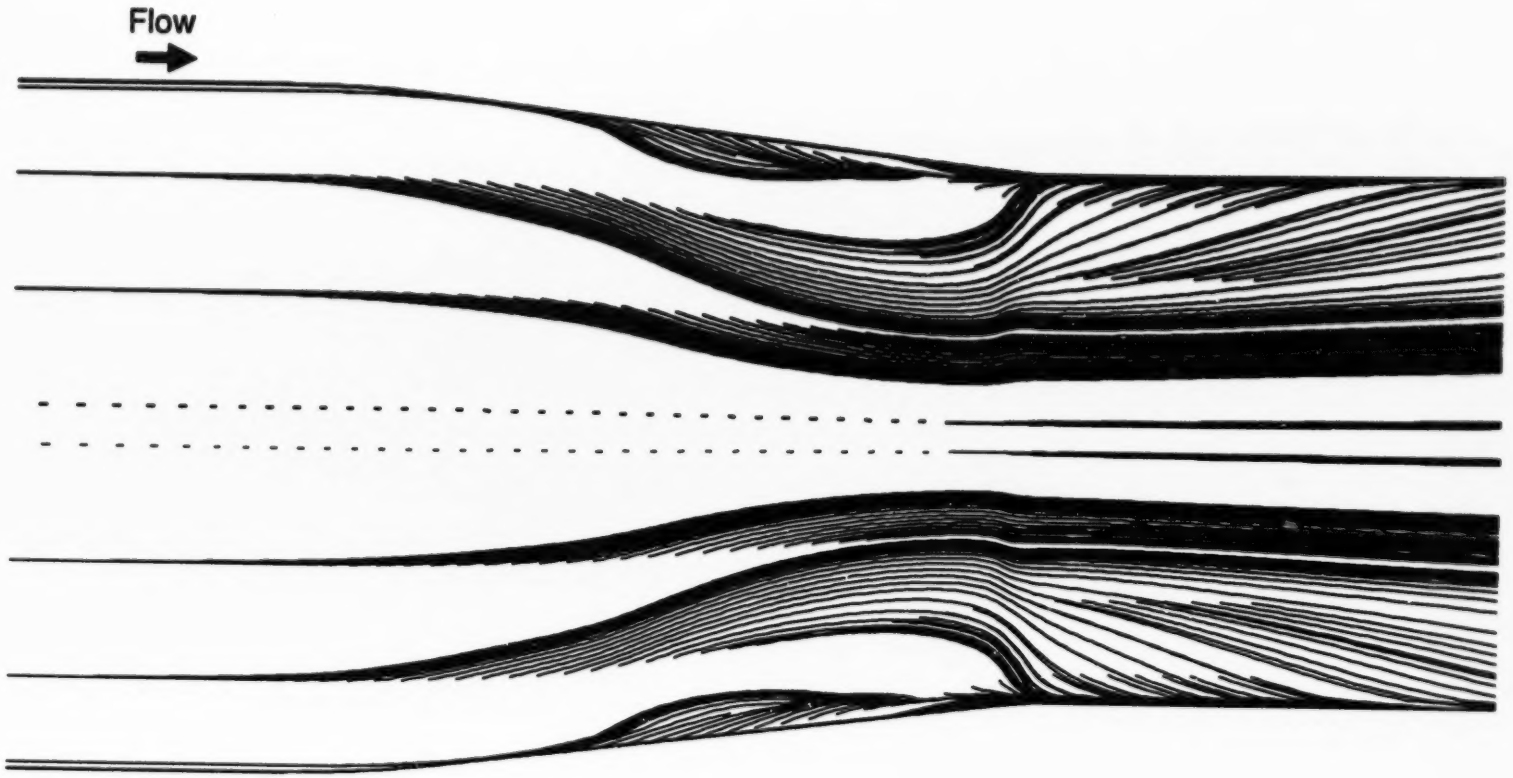

(a) Top view.

Figure 12. Particle traces next to surface (computed oil flows). $M_\infty = 0.80$; turbulent flow; $R_\ell = 19.5 \times 10^6$; fine grid.

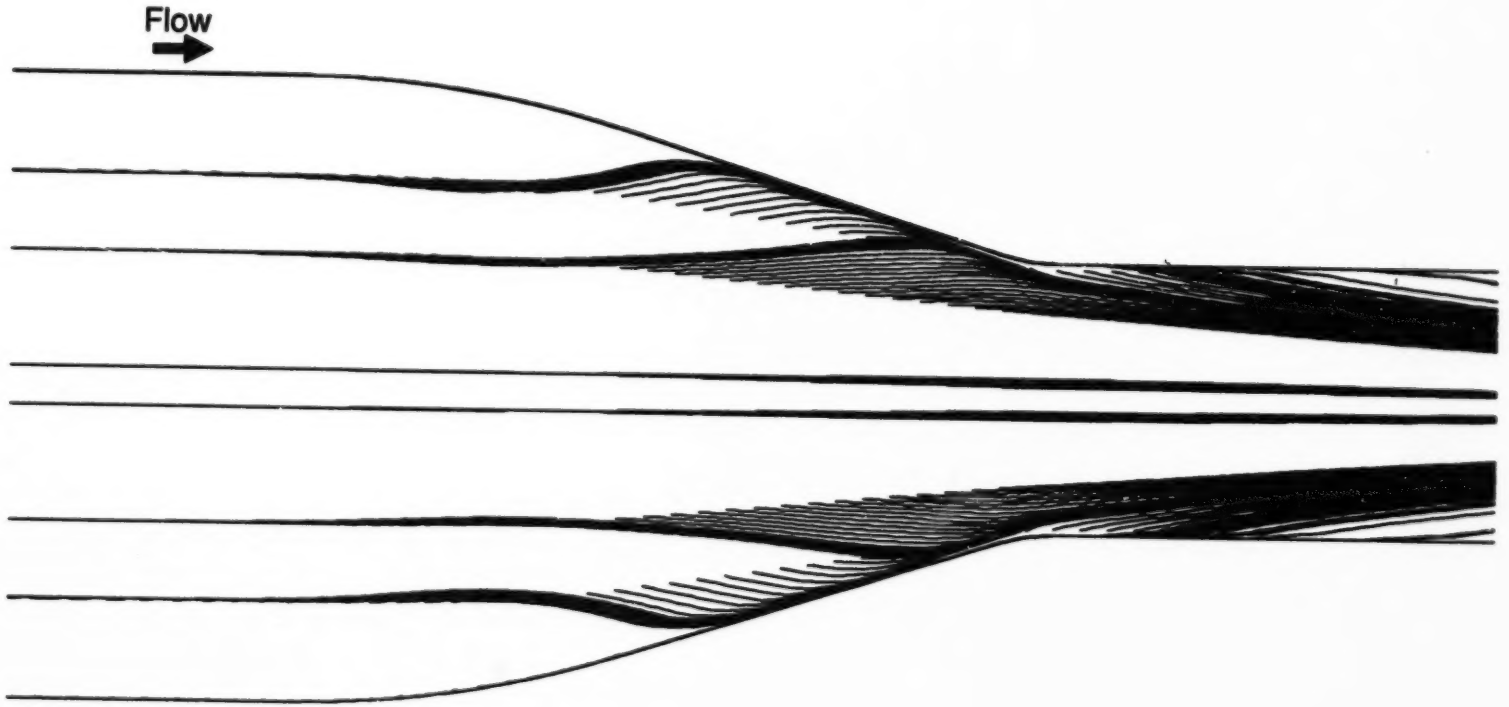

(b) Side view.

Figure 12. Concluded.

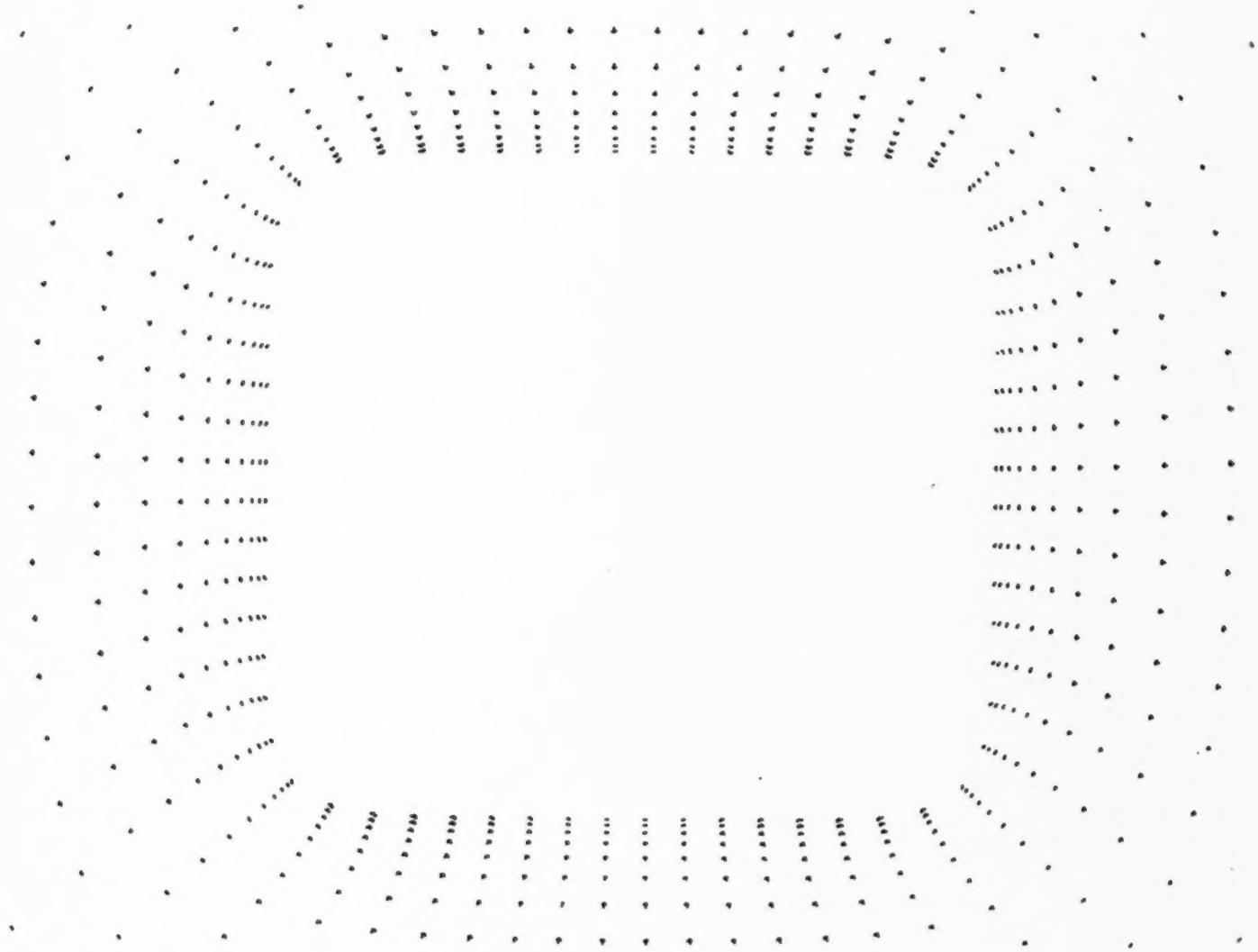

(a) $x/l = 0.44$ (start of boattail).

Figure 13. Cross-flow velocity vectors. Looking upstream; $M_\infty = 0.80$; turbulent flow; $R_\ell = 19.5 \times 10^6$; fine grid.

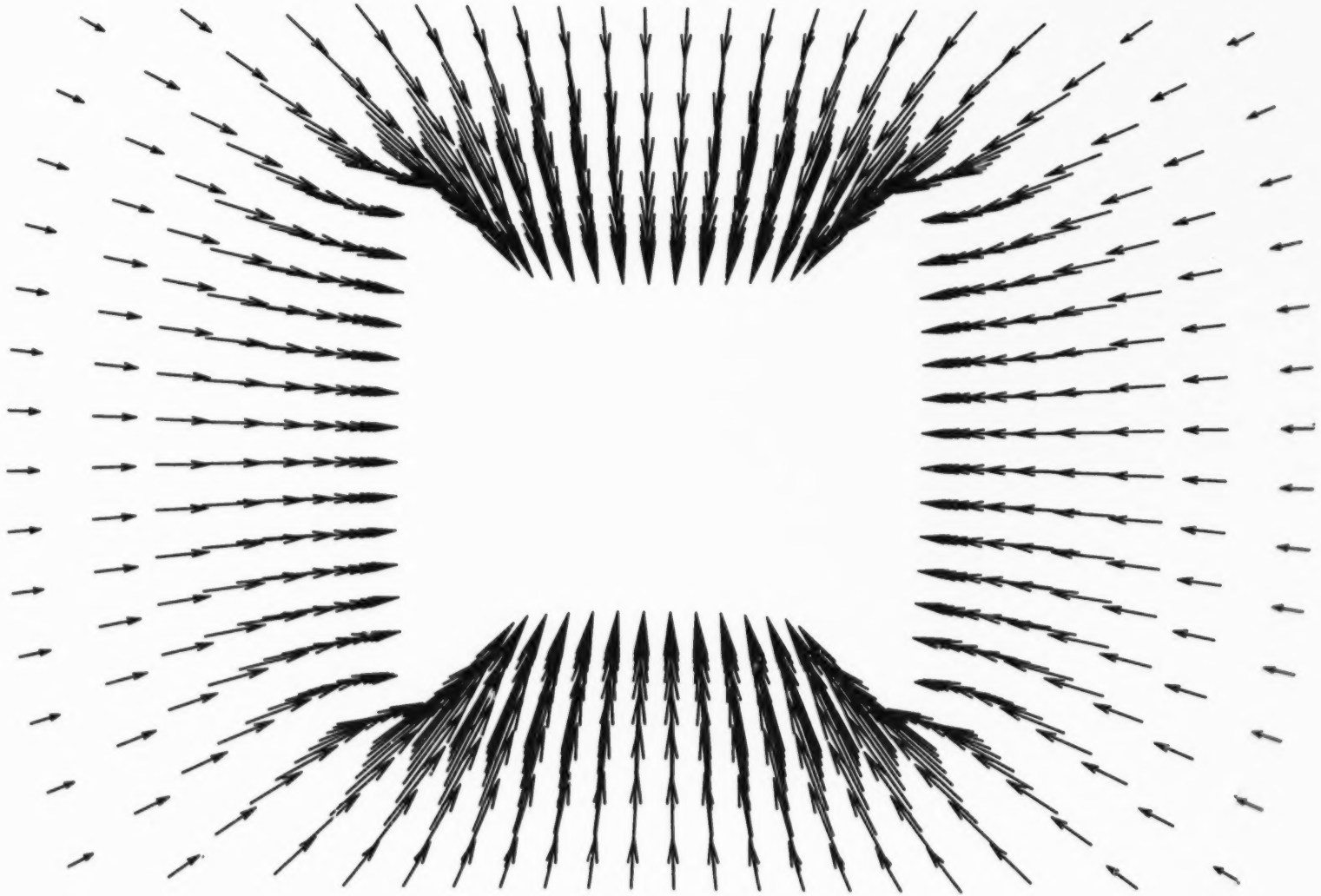

(b) $x/l = 0.46$.

Figure 13. Continued.

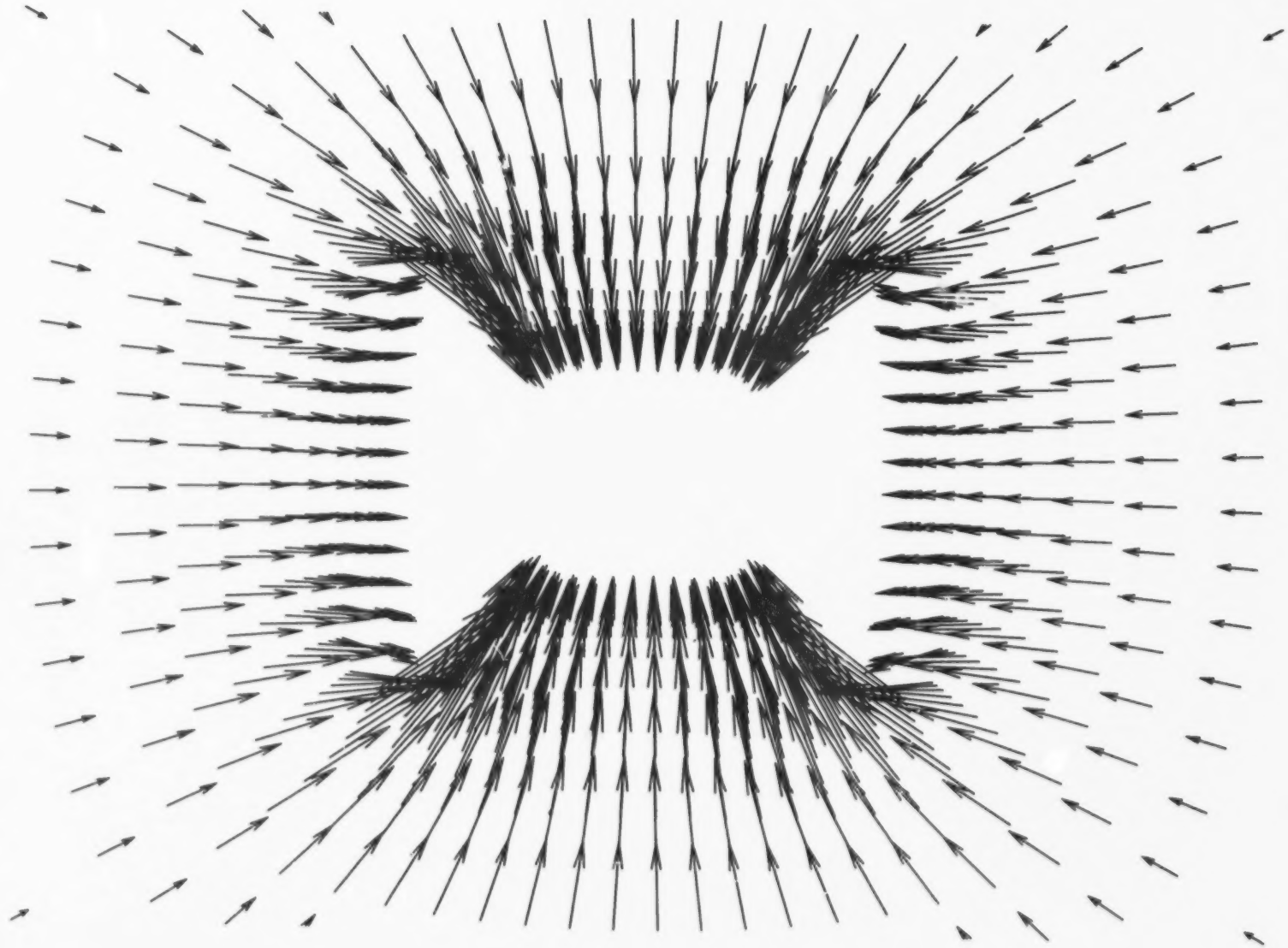

(c) $x/l = 0.48$.

Figure 13. Continued.

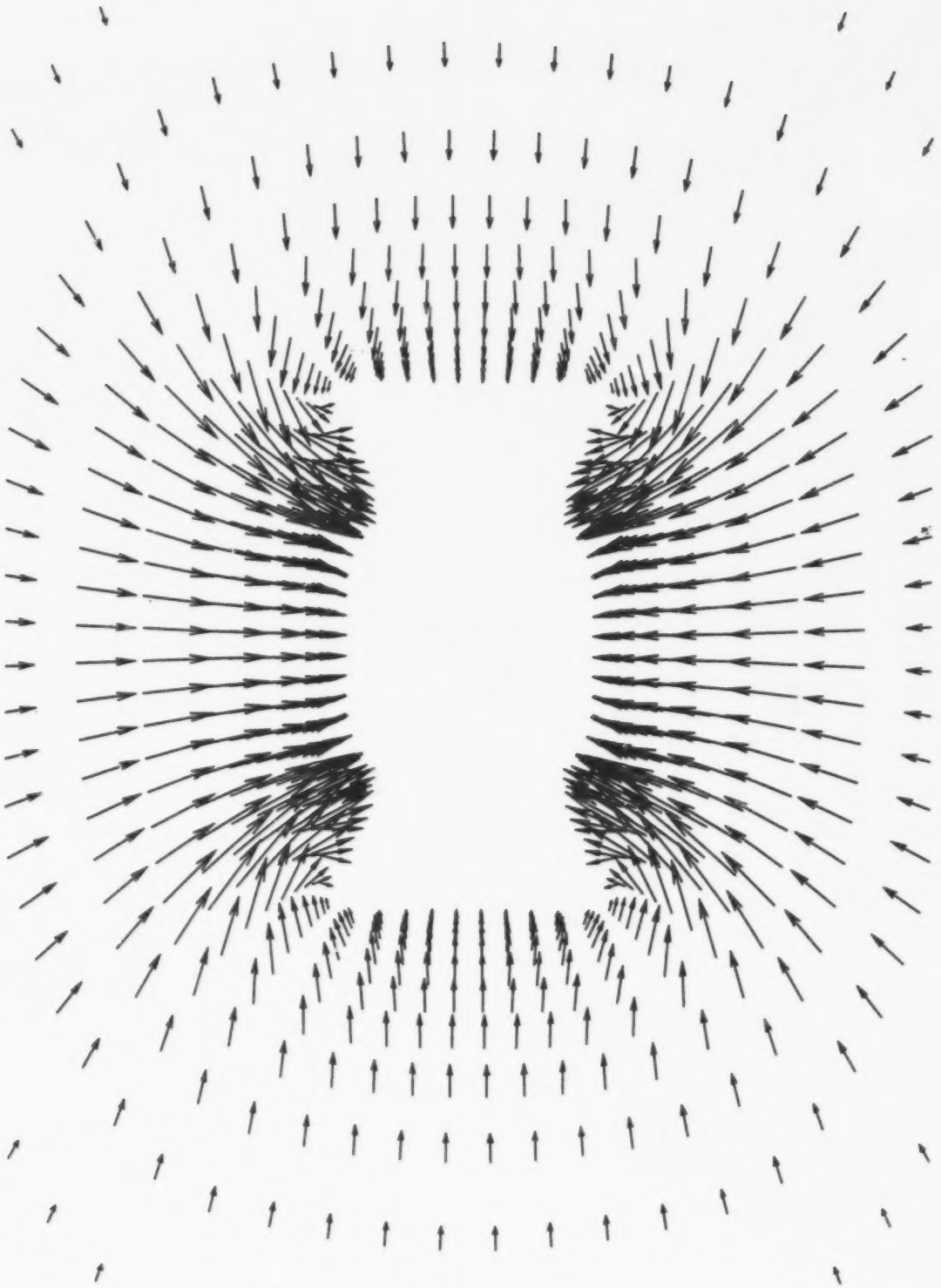

(d) $x/l = 0.50$ (nozzle exit).

Figure 13. Continued.

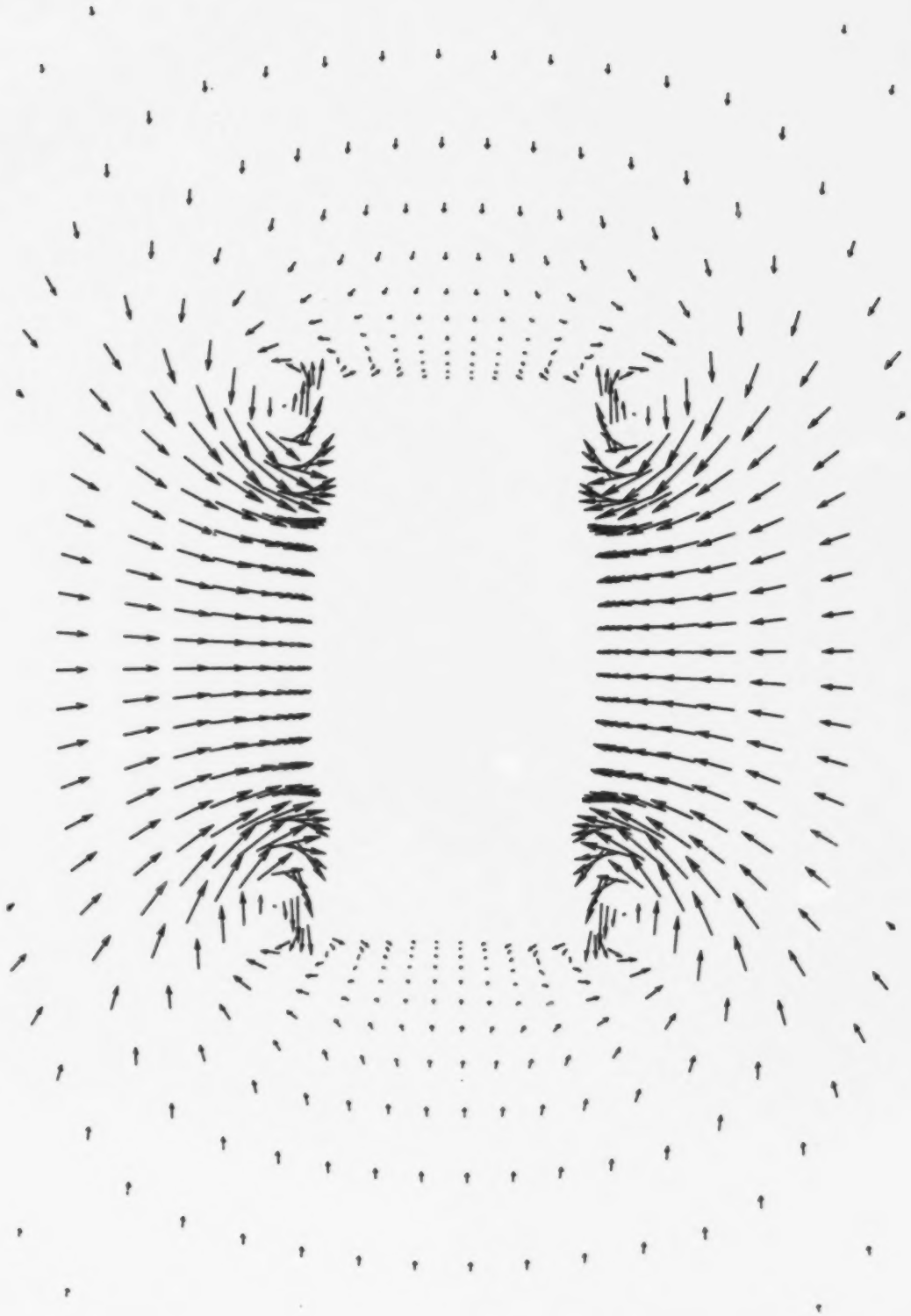

(e) $x/l = 0.52$.

Figure 13. Continued.

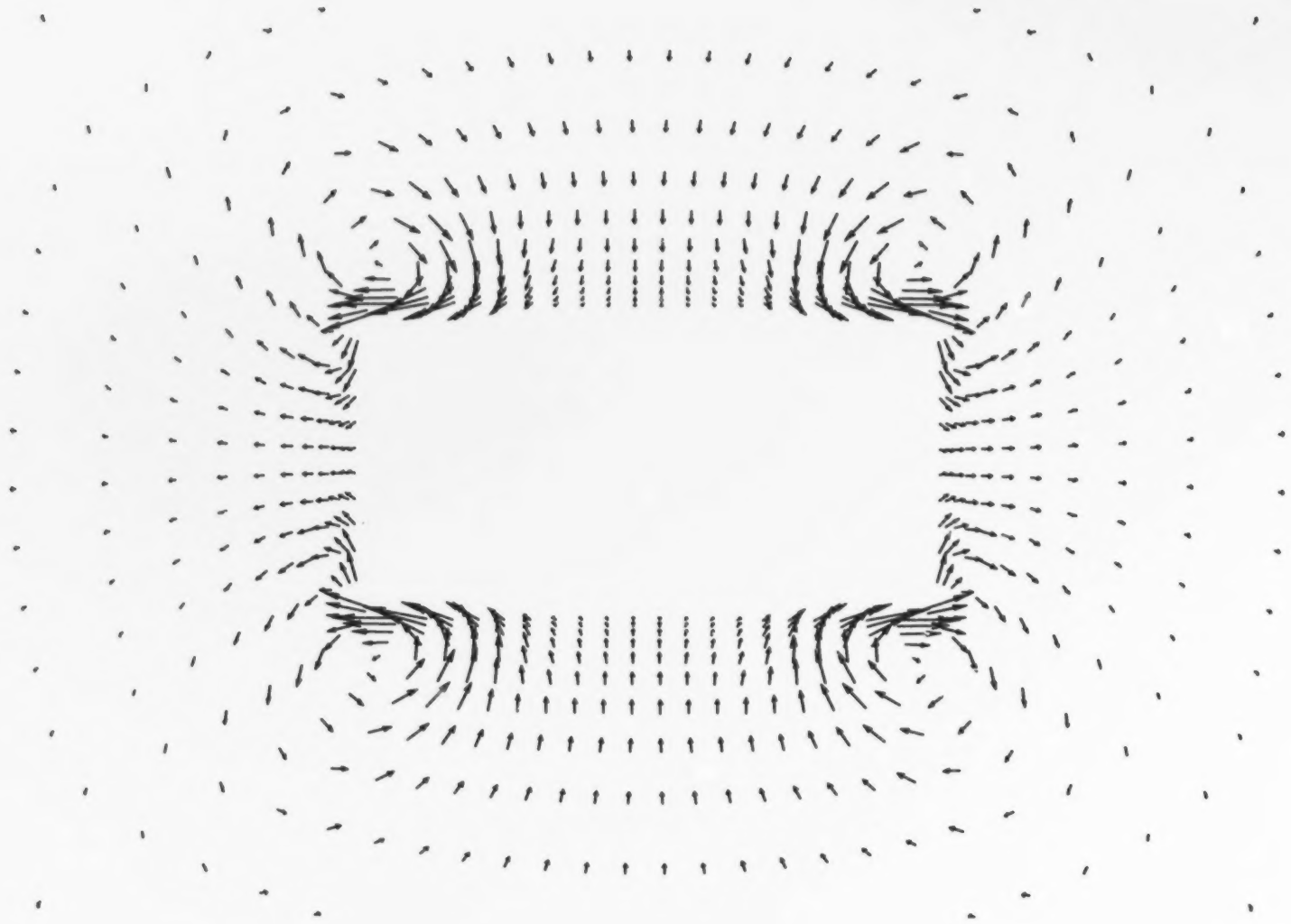

(f) $x/l = 0.54$.

Figure 13. Continued.

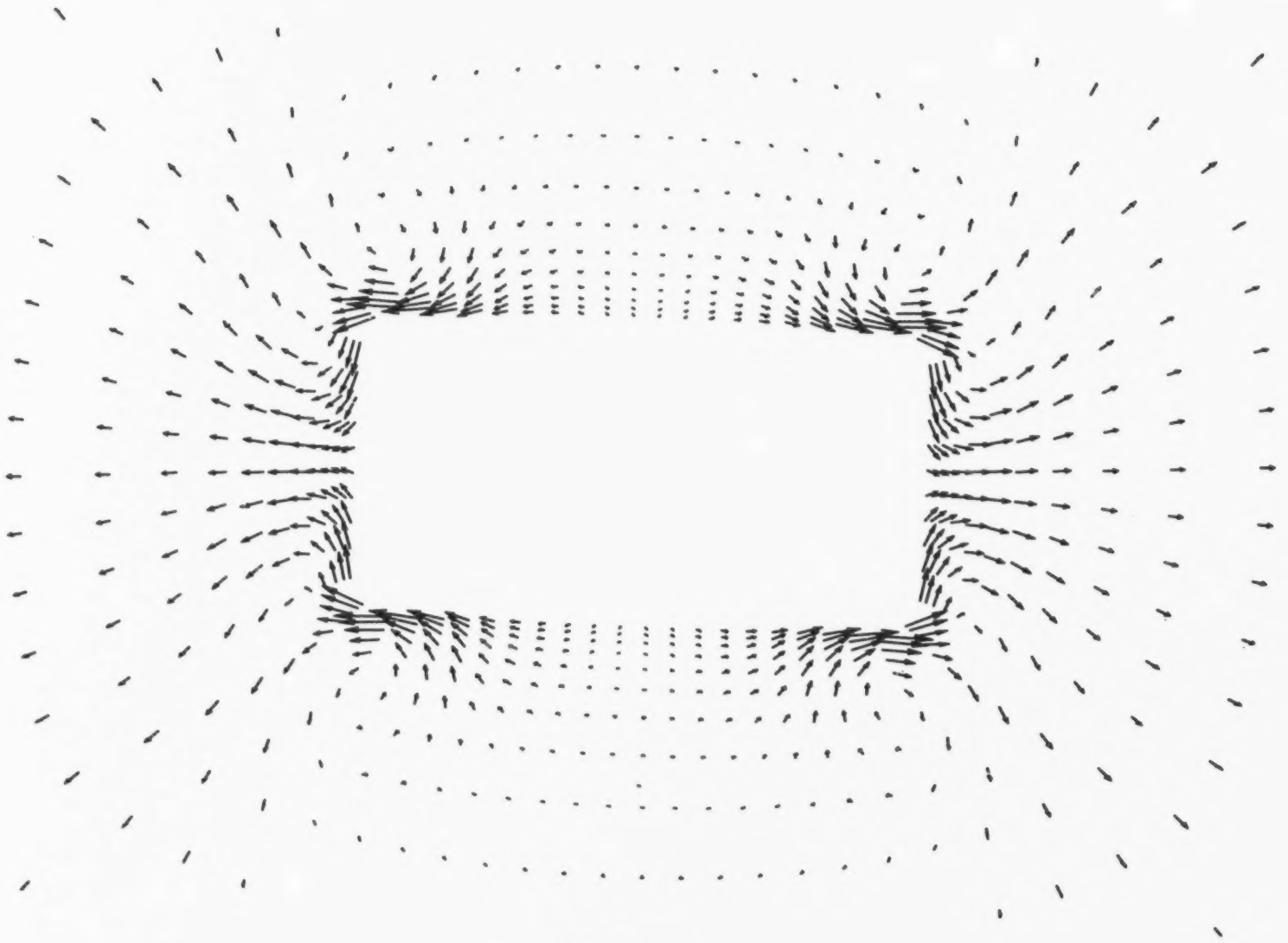

(g) $x/l = 0.61$.

Figure 13. Concluded.

NASA
National Aeronautics and Space Administration

Report Documentation Page

1. Report No.	2. Government Accession No.	3. Recipient's Catalog No.
NASA TM-4111		

4. Title and Subtitle
Transonic Navier-Stokes Solutions of Three-Dimensional Afterbody Flows

5. Report Date
July 1989

6. Performing Organization Code

7. Author(s)
William B. Compton III, James L. Thomas, William K. Abeyounis, and Mary L. Mason

8. Performing Organization Report No.
L-16516

9. Performing Organization Name and Address
NASA Langley Research Center
Hampton, VA 23665-5225

10. Work Unit No.
535-03-01-01

11. Contract or Grant No.

12. Sponsoring Agency Name and Address
National Aeronautics and Space Administration
Washington, DC 20546-0001

13. Type of Report and Period Covered
Technical Memorandum

14. Sponsoring Agency Code

15. Supplementary Notes

16. Abstract

The performance of a three-dimensional Navier-Stokes solution technique in predicting the transonic flow past a nonaxisymmetric nozzle has been investigated. The investigation was conducted at free-stream Mach numbers ranging from 0.60 to 0.94 and an angle of attack of 0°. The numerical solution procedure employs the three-dimensional, unsteady, Reynolds-averaged Navier-Stokes equations written in strong conservation form, a thin layer assumption, and the Baldwin-Lomax turbulence model. The equations are solved by using the finite-volume principle in conjunction with an approximately factored upwind-biased numerical algorithm. In the numerical procedure, the jet exhaust is represented by a solid sting. Wind-tunnel data with the jet exhaust simulated by high pressure air were also obtained to compare with the numerical calculations.

17. Key Words (Suggested by Authors(s))
Navier-Stokes
Afterbody
Nozzle
Numerical
Three-dimensional
Transonic

18. Distribution Statement
Unclassified—Unlimited

Subject Category 02

19. Security Classif. (of this report)	20. Security Classif. (of this page)	21. No. of Pages	22. Price
Unclassified	Unclassified	59	A04

NASA FORM 1626 OCT 86

NASA-Langley, 1989

For sale by the National Technical Information Service, Springfield, Virginia 22161-2171